



THREE CHANNEL POLARIMETRIC BASED DATA DECONVOLUTION

THESIS

Kurtis G. Engelson, Captain, USAF
AFIT/GE/ENG/11-10

**DEPARTMENT OF THE AIR FORCE
AIR UNIVERSITY**

AIR FORCE INSTITUTE OF TECHNOLOGY

Wright-Patterson Air Force Base, Ohio

APPROVED FOR PUBLIC RELEASE; DISTRIBUTION UNLIMITED

The views expressed in this thesis are those of the author and do not reflect the official policy or position of the United States Air Force, Department of Defense, or the United States Government. This material is declared a work of the U.S. Government and is not subject to copyright protection in the United States.

THREE CHANNEL POLARIMETRIC BASED DATA DECONVOLUTION

THESIS

Presented to the Faculty

Department of Electrical and Computer Engineering

Graduate School of Engineering and Management

Air Force Institute of Technology

Air Education and Training Command

In Partial Fulfillment of the Requirements for the
Degree of Master of Science in Electrical Engineering

Kurtis G. Engelson, B.S.E.E.

Captain, USAF


March 2011

APPROVED FOR PUBLIC RELEASE; DISTRIBUTION UNLIMITED

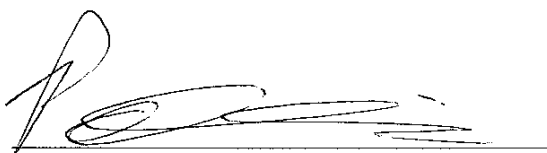
THREE CHANNEL POLARIMETRIC BASED DATA DECONVOLUTION

Kurtis G. Engelson, B.S.E.E
Captain, USAF

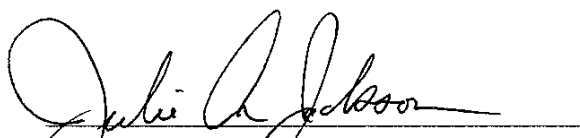
Approved:


Stephen C. Cain (Chairman)

9 March 2011
Date


Patrick S. Chapin (Member)

9 March 2011
Date


Julie A. Jackson (Member)

9 March 2011
Date

Abstract

A three channel polarimetric deconvolution algorithm was developed to mitigate the degrading effects of atmospheric turbulence in astronomical imagery. Tests were executed using both simulation and laboratory data. The resulting efficacy of the three channel algorithm was compared to a recently developed two channel approach under identical conditions ensuring a fair comparison amongst both algorithms. Two types of simulations were performed. The first was a binary star simulation to compare resulting resolutions between the three and two channel algorithms. The second simulation measured how effective both algorithms could deconvolve a blurred satellite image. The simulation environment assumed the key parameters of Fried's Seeing parameter, r_0 , and telescope lens diameters of D_1 and D_2 . The simulation results showed that the three channel algorithm always reconstructed the true image as good as or better than the two channel approach, while the total squared error was always significantly better for the three channel algorithm. The next step is comparing the two algorithms in the laboratory environment. However, the laboratory imagery was not actually blurred by atmospheric turbulence, but instead camera defocusing was used to simulate the blurring that would be caused by atmospheric turbulence. The results show that the three channel significantly outperforms the two channel in a visual reconstruction of the true image.

Table of Contents

1.	Introduction.....	1
1.1	Motivation for Research and Applications.....	1
1.2	Problem Statement	2
1.3	Scope of Research Effort	3
1.4	Chapter Summaries	4
2.	Background.....	6
3.	Simulation Description	9
3.1	Convolution Model	9
3.1.1	Optical Transfer Function Model	10
3.1.2	Noise Model	12
3.1.3	Simulating Image Degradation.....	13
3.2	Deconvolution Model.....	17
3.2.1	The Update Equations	18
3.2.2	Partial 3 Channel Polarimeter Derivation.....	19
3.2.3	Point Source Pixel Spacing	25
4.	Simulation Results	27
4.1	Dual Point Source	27
4.1.1:	160 cm Lens Results.....	28
4.1.2:	120 cm Lens Results.....	29
4.2	Satellite Image.....	30
4.2.1:	160 cm Lens Results.....	31
4.2.2:	120 cm Lens Results.....	31

5.	Laboratory Imagery Results	34
5.1	Laboratory Setup	34
5.2	Laboratory Image Blur and Noise	34
5.3	Laboratory Results	37
6.	Limitations	38
6.1:	ratio.....	38
6.2:	No Blind Deconvolution:	38
6.3:	Lack of Algorithmic Autonomy (no stopping criteria)	38
6.4:	Diversity of Multi-Channel Data due to Polarization.....	40
7.	Conclusions	41
	Appendix A: 3 Channel Polarimetric Data Deconvolution Algorithm Derivation	A - 42 -
	Appendix B: Derivation for Assumed Poisson Noise in Richardson Lucy Algorithm	B - 54 -
8.	Bibliography	- 57 -

List of Figures

Figure	Page
1.1: Effect of Atmospheric Turbulence	3
2.1: Literature Review Timeline	8
3.1: Convolution Model Diagram	10
3.2: Random photon arrivals cause of photon counting noise	13
3.3: Example set of a 3 Channel Polarimeter	14
3.4: Logical flow of data degradation process	15
3.5: Example of binary star pattern degraded by Poisson noise and blurring from h_{sys}	15
3.6: Deconvolution algorithm flow chart	18

3.7: Point source pixel spacing	25
4.1: Binary star 160cm lens simulation results	28
4.2: Binary star 120cm lens simulation results	29
4.3: Binary star results comparison for high iterations	30
4.4: Satellite image, polarized data, and measured data for 160cm lens	31
4.5 Satellite image simulation results for 160cm lens	31
4.6: Satellite image, polarized data, and measured data for 120cm lens	31
4.7: Satellite image simulation results for 120cm lens	32
4.8: 3vs2 Channel comparison at 6 pixel separation	33
5.1: Laboratory experiment setup	34
5.2: Lab data true image and blurred image	35
5.3: OTF comparison for lab data and simulation data	36
5.4: Lab results 3 CH vs. 2 CH	37
6.1: Likelihood of 3 CH object at 300k iterations	39
6.2: Total squared error of 3CH object at 448k iterations	40

List of Tables

Table	Page
3.1: Variable Equivalencies Table	16
3.2: Definitions of variables used in 3 CH deconvolution algorithm	20
4.1: 160 cm lens results	28
4.2: 120 cm lens results	29

List of Acronyms

Acronym

APD	Avalanche Photo Diode
CCD	Charged Coupled Device

DoD	Department of Defense
LED	Light Emitting Diode
EM	Expectation Maximization
LEOTF	Long Exposure Transfer Function
MAP	Maximum a Posteriori
MSSS	Maui Space Surveillance Site
OTF	Optical Transfer Function
PDF	Probability Density Function
PMF	Probability Mass Function
PSF	Point Spread Function
SNR	Signal to Noise Ratio
TSE	Total Squared Error

Three Channel Polarimetric Data Based Deconvolution

1. Introduction

1.1 Motivation for Research and Applications

Polarimetric imaging in astronomy offers one distinct advantage when compared to standard imaging techniques. This advantage arises when imaging man-made objects, because of the tendency for these objects to reflect polarized light more than its surroundings. The polarized data that is collected from objects in space can be very beneficial in image analysis, and is proven in this research. However, polarimetric imaging performance is limited by the blurring caused by the atmosphere. Therefore, it is very beneficial to combine polarimetry with an image processing technique known as deconvolution to deblur images degraded by the atmospheric conditions.

One of the main goals of this research is to develop a three channel polarimetric deconvolution algorithm with superior resolving capability to that of the prior researched two channel approach [6]. A two point resolution metric is used in this research to determine which imaging technique is superior. The technique is similar to that used by Lord Rayleigh in that resolution is determined by the ability to resolve two point sources [3]. A majority of simulations and critiques to the algorithm proposed in this thesis were centered on the idea of resolving two point sources. The efficacy of the deconvolution algorithm to resolve two point sources is directly related to how well it will deconvolve a more complex image, such as a satellite image.

Another goal of this research is to not only resolve sharper images, but also to collect and estimate polarization data from an object in observation. Polarization data can be used specifically to assist in identifying a target, or more generally to identifying materials [5]. The proposed algorithm is capable of estimating a parameter defined as the polarization attenuation factor. This factor is mathematically dependent on the angle of polarization of the light reflected by the material in the observation. The angle of polarization data is the potentially useful information in identification of materials or targets.

The capability to analyze sharper astronomical images and corresponding polarization data can prove to be very useful for the United States Air Force. As the DoD's perception of war in space evolves it is necessary that we always maintain space superiority. Cutting edge surveillance, intelligence, and reconnaissance are imperative to attaining space superiority, and that is where this research potentially contributes. For example, someday it may be very useful to closely monitor our satellites and enemy satellites. Satellites in extreme distant orbits (Geostationary) do not return much light and provide very dim and low resolution images. If an enemy satellite was in close proximity to our own satellite, we may be interested to know that. Unfortunately, an image from current telescopes may not show a distinction between two satellites in relatively close proximity, but more likely will blur them together into one mass of light. However, if polarimetry in conjunction with deconvolution is used it may become more apparent that there are two satellites instead of one. The deconvolution provides for more clarity in the image by deblurring, while the polarization information can help in determining if the object in observation is man-made. This type of capability is just one example of how the USAF can retain space superiority.

1.2 Problem Statement

One major problem with imaging objects in space is the negative effects the atmosphere introduces into the imaging process. Specifically, atmospheric turbulence causes aberrations in images when viewed from the surface of earth [12:69]. Figure 1.1 demonstrates the problem presented by atmospheric turbulence. This scenario shows a star that is a great distance away from the earth. The light from the star will naturally radiate in a spherical manner, but as it travels a distance of "near infinity" it becomes a plane wave. As the wave enters the earth's atmosphere it starts out flat, but as it travels through the phase front changes and becomes degraded.

Atmospheric turbulence causes time delays in the light wave as it passes through the atmosphere, but the delay is not uniform across the entire plane wave. The tilt illustrates how the right portion of the light passes through after the left side. This delay will inevitably have an effect on the image formed at the detector of camera, which is on the other side of the lens of a telescope. The lens of the telescope will cause all incoming light outside to converge as shown towards the detector. An ideal scenario would be that the light comes in untilted and forms an image centered on the detector, but in reality this is not the case. An input of tilted light on a lens will result in a shifted image on the corresponding detector, based on the shift theorem of Fourier transforms [3:8]. After a "long" exposure time, there will not be just one shift of the point source, but an accumulation of many shifts, which appear

as blur in the image. There are other aberrations in the imagery due to atmospheric effects, but tilted light is the dominant source of blurring in long exposure astronomical imagery [12:69]. Image A in Figure 1.1 shows a simulated example of an ideal image of two point sources (top of figure), and the resulting blurry measured image at the detector (Image B). The bottom image in the figure will be referred to from now on as measured data $d(x,y)$.

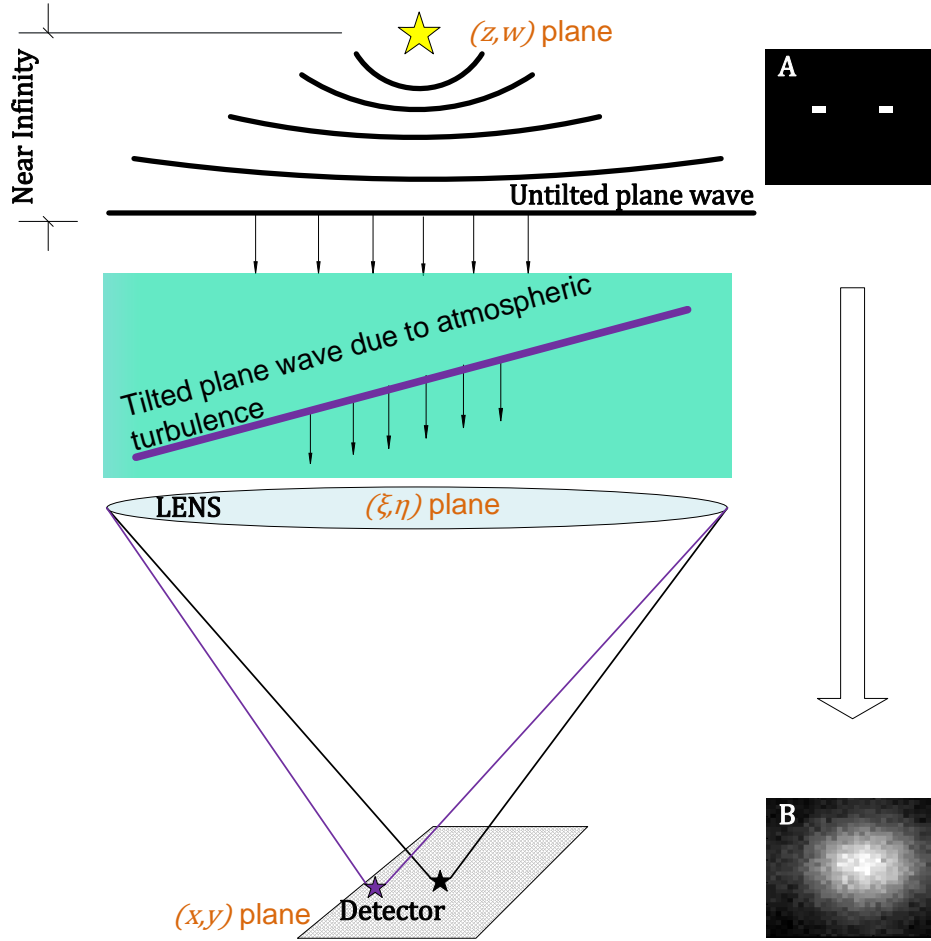


Figure 1.1: Left-Instantaneous example of the consequences of atmospheric turbulence on a traditional non-polarimetric imaging system. Image A- Example of two binary star true intensity. Image B- Example of data measured on camera detector known as measured data

1.3 Scope of Research Effort

The goal of this research is to provide an effective three channel polarimetric deconvolution algorithm for reconstructing images which have been degraded by atmospheric turbulence and noise. This thesis explains in entirety the process used for deblurring and de-noising images. Results are shown for both simulation and laboratory data.

1.4 Chapter Summaries

Chapter 1: Introduction

This chapter introduces the topic of three channel polarimetric imaging, by first explaining the motivation and applications of it. It then gives a concise problem statement, followed by the scope of this actual research effort.

Chapter 2: Background

Chapter 2 provides a chronological background of all the research performed in the last four decades, which have significantly contributed to the research effort described in this thesis.

Chapter 3: Simulation Description

A description of the simulation is the most important part of this thesis. Chapter 3 starts by introducing the convolution model, which addresses how an ideal image is degraded. The convolution model is broken up into three subsections: an explanation of optical transfer functions, the noise model, and a section to explain how an image is actually degraded via a process explanation. The second subsection to Chapter 3 is the deconvolution model, which explains the process for inverting the convolution model. It starts by introducing the process of deconvolution, and then transitions into a more technical discussion of the equations and derivation necessary to have a functional deconvolution algorithm. It finishes with a brief discussion on dual point source pixel spacing for the ideal image in simulation.

Chapter 4: Simulation Results

The simulation results section is broken up into two major parts. The first section addresses the simulation results for dual point sources, and the second discusses the results for simulations executed with an ideal satellite image. It is shown in all simulation cases that the three channel algorithm outperforms or performs the same as the two channel in aesthetics, while the three channel always outperforms in total squared error calculations.

Chapter 5: Laboratory Imagery Results:

Laboratory imagery is the final step taken in this thesis to compare both algorithms. This section explains the laboratory set up, image degradation model, and analysis of results. The results show that the three channel algorithm outperforms the two channel algorithm.

Chapter 6: Limitations

The limitations chapter explains potential limitations of the three channel algorithm either in simulation scenarios or laboratory data scenarios. The four limitations explained are the effect of lens diameter to seeing parameter () ratio, the absence of blind deconvolution, lack of algorithmic autonomy, and diversity of multi-channel data due to polarization.

2. Background

William Richardson began the modern era of deconvolution in image processing when he published an algorithm that was dependent on Bayes's Theorem. He describes in his journal article *Bayesian-Based Iterative Method of Image Restoration* [11] how an image degraded by a point spread function can be restored to a near perfect original image all through use of Bayes' theorem. He built the framework for many future researchers when he derived an iterative approach of applying Bayes's theorem to estimate the true values of an image given the degraded image and a known point spread function. In 1974 Lucy also devised a clever use of Bayes's theorem in application to estimation theory and he took it one step further by including the concepts of maximum likelihood in his estimation process [10]. Lucy's work and concepts were applied to astronomy, but not astronomical imaging, which is the topic of this research effort.

In 1976 Dempster, Laird and Rubin wrote a journal article for the Royal Statistical Society called, *Maximum Likelihood from Incomplete Data via the EM Algorithm* [1], which had a tremendous impact in image processing theory. In it they describe a process called the Expectation Maximization (EM) process. The paper presents an iterative approach to maximum likelihood estimation with the observed data being referred to as incomplete data. The EM process is dependent on two types of data, the first being incomplete data and the other complete data. The complete data is an abstract idea and its relevance and application to this research is explained later in 3.2.2. The process was termed the EM process because each iteration has two key steps. The first is the expectation step, and the second is the maximization step [1]. These steps are also more clearly defined with respect to this research in 3.2.2.

In 1982 Shepp and Vardi wrote an article on emission tomography, where they used concepts of maximum likelihood estimation and EM to reconstruct images. This document is a major source of interest for this research because of the developments these two men made in application of the EM process [14]. Specifically, their results for how to define the conditional expectations were used later by Timothy Schulz in his research [13]. The mathematical model developed throughout this thesis is most closely related to the work described by Schulz in his 1993 Joint Optical Society of America article [13]. Section 3.3.2 details the mathematical model used in this research and a detailed discussion of the similarities and differences between Schulz's model and our own.

About thirteen years later in 2006 Major Dave Strong continued researching in the application of the EM process to astronomical imaging. He advanced Schulz's research one step further and developed a two channel polarimeter, which used one channel of unpolarized light and one channel of linearly polarized light. His solution was also restricted to short exposure imagery as was Schulz's [15].

Soon after Strong finished his dissertation, Daniel LeMaster researched in the field of polarimetric imaging. In 2007 LeMaster researched a similar three channel approach to what has been developed in this research, but there are some critical differences [8]. First and most importantly, he was only researching deconvolution algorithms for short exposure imagery, where this effort only considered long exposure imagery. LeMaster also used different polarization analyzer settings (0° , 60° , -60°) than used in the three channel approach described throughout this thesis (0° , 45° , 90°). The difference in polarization analyzer settings determines a different derivation resulting in a different deconvolution algorithm. He also directly estimated the angle of polarization of the light in his deconvolution algorithm, where he discovered that the estimates of the angles of polarization are very susceptible to noise and time consuming to obtain. The deconvolution algorithm developed in this research does not estimate the angle of polarization, but it does estimate the polarization attenuation factors, which are dependent on the angle of polarization. Estimating this parameter may prove to be less susceptible to noise and require fewer mathematical steps. This concept is further explained in 3.1.3 and 3.2.2.

LeMaster was able to effectively restore images using the developed three channel deconvolution algorithm, but he was never able to effectively estimate the angle of polarization. LeMaster's dissertation [8] also lacked one important thing and that was a comparison of a three channel versus two channel algorithm. Conversely, this research effort is focused on a comparison of three channel versus two channel algorithm. The two channel algorithm compared to was developed by Captain Steve James in 2008 [6]. In his research he developed a two channel polarimeter deconvolution algorithm capable of restoring images corrupted by noise and blurring. His algorithmic solution was determined through use of a Bayesian estimation method called maximum a posteriori (MAP) estimation [7: 350]. He also utilized the concepts of complete and incomplete data, which are defined in the EM process [1], [7: 187]. It was through the use of MAP estimation and the EM algorithm that he was able to develop a deconvolution algorithm capable of restoring images to a less noisy and blurred state. The three channel approach described in this thesis closely mimics his strategy of using MAP estimation in conjunction with the EM

process, but requires a different mathematical derivation to arrive at the update equations inside the deconvolution algorithm.

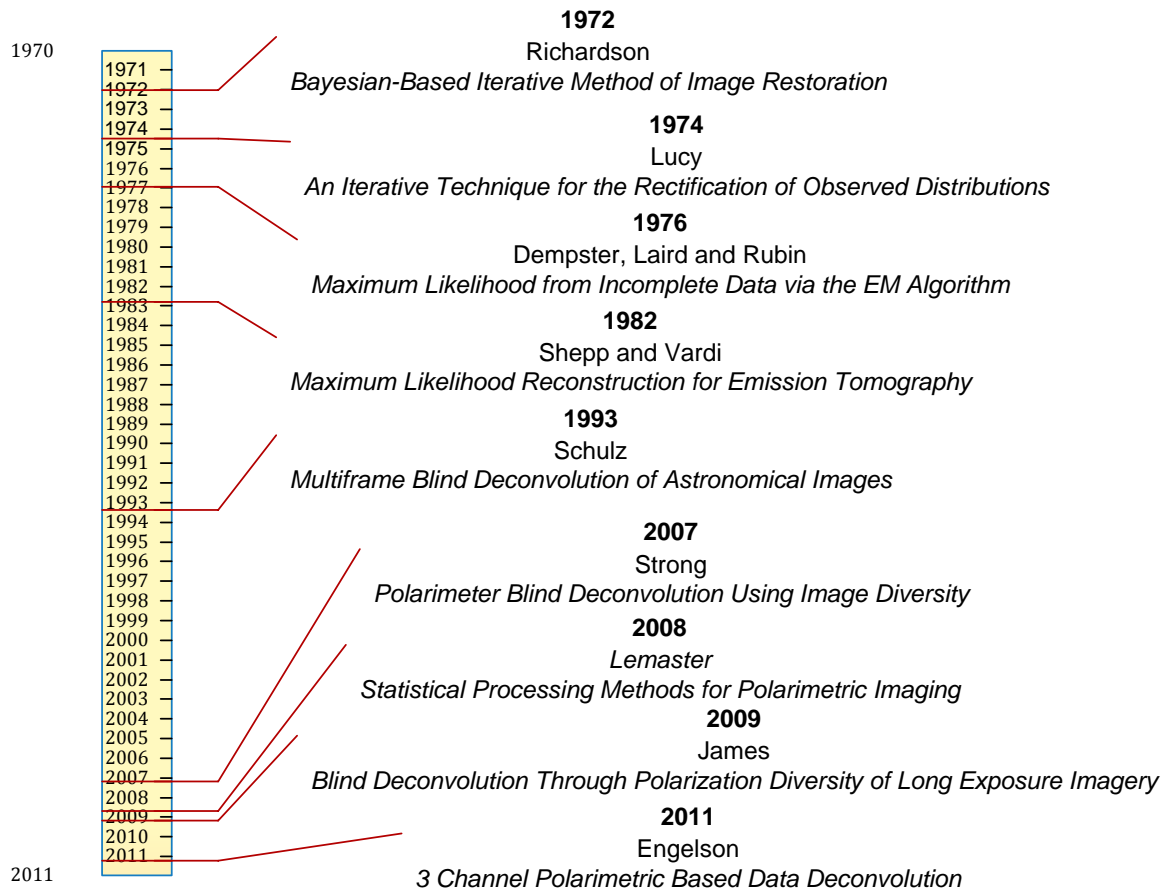


Figure 2.1: Literature Review Timeline: chronologically displays contributions used to develop and execute 3 channel polarimetric deconvolution of astronomical images.

3. Simulation Description

3.1 Convolution Model

This section addresses the transformation process of ideal true intensity to the blurred and noisy measured data. First, the idea of true intensity must be understood. One example of true intensity can be seen in Image A of Figure 3.1, where there is an image of two binary stars. It is called true intensity because it is a perfect and unaberrated image. It is also the benchmark data set used to compare results to later on.

Figure 3.1 demonstrates the process by which the true intensity is processed by a camera. It also provides a block diagram of the optical system, where the input is true intensity convolved with the system point spread function (PSF). Due to the properties of linearity and shift invariance the system can be characterized by the PSF, as an electrical system can be characterized by its impulse response [3:19]. The system PSF is a combination of the long exposure PSF, h_{LE} , convolved with optics based PSF, h_{OB} (refer to Equation (3.4)). The measured data I_m is the result of a convolution of true intensity with h_{OB} plus noise. The blurry but non-noisy image I_b is related to the true intensity, I_t , via equation:

(3.1)

It is space invariant because h_{OB} only depends on the distances between points (x_1, y_1) and (x_2, y_2) , where (x, y) is the detector plane coordinates and (x_o, y_o) is the observation plane coordinates [3:18-21].

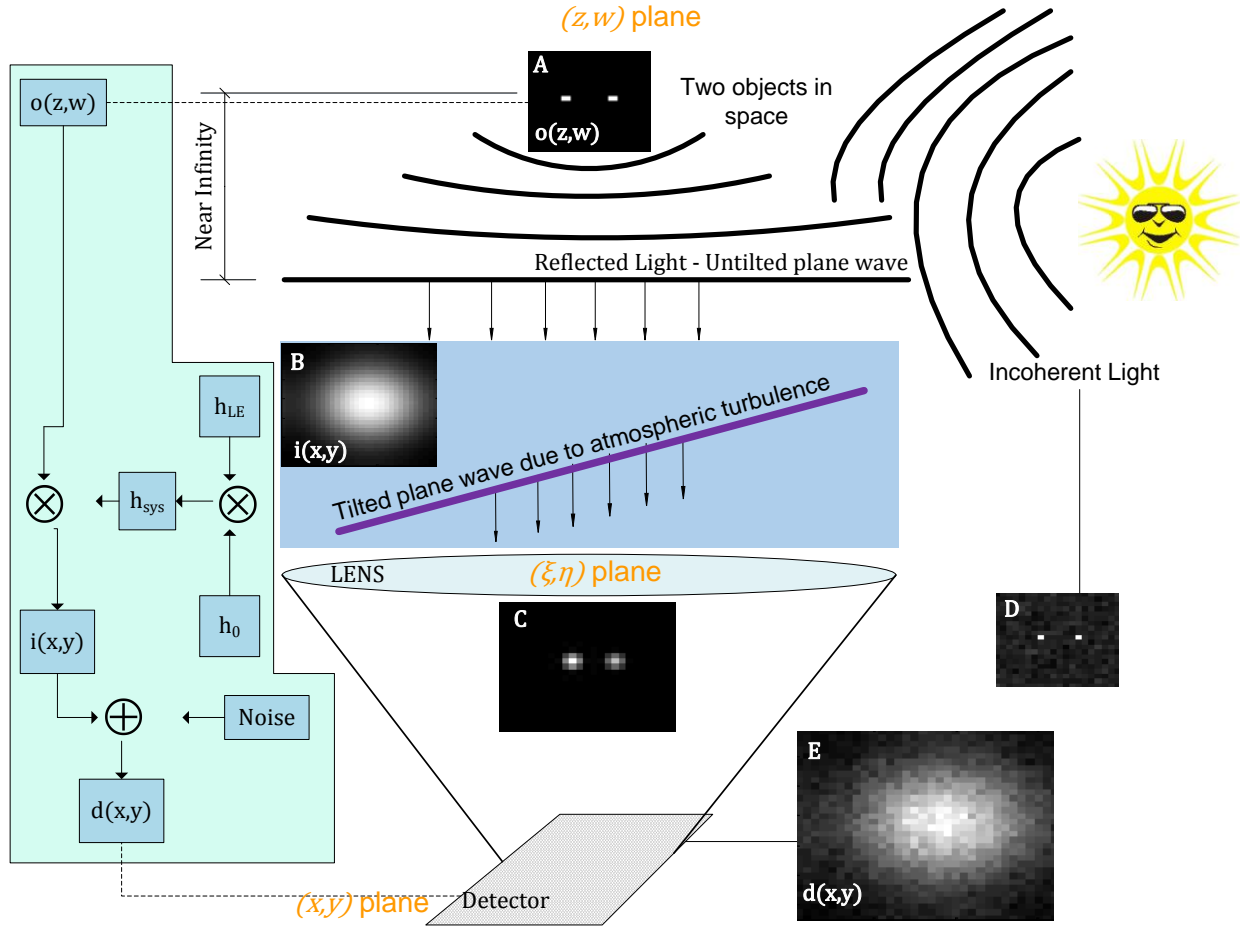


Figure 3.1: A continuation of Figure 1 with the deconvolution model boxed off to the left. Image A- True intensity. Image B- True intensity blurred with long exposure transfer function . Image C- True intensity blurred with optics based OTF . Image D- True intensity with added Poisson modeled noise. Image E- Data measured at camera detector .

3.1.1 Optical Transfer Function Model

There are two sources of blurring specifically considered in this research in the degradation process of the data. Image B in Figure 3.1 demonstrates the first source of blurring is caused by atmospheric turbulence. The blurring caused by atmospheric turbulence is modeled with the long exposure optical transfer function (LEOTF), which is the Fourier transform of the PSF . It is the cause for the most severe degradation to the true intensity. This OTF is only used in long exposure imagery (). If short exposure imagery were relevant to this research as it was to some of the previous efforts discussed in section 2, then the OTF would be modeled with a different equation than the LEOTF. The formula for the LEOTF is given by Equation (3.2) [2:402,439]. Notice that

the resulting magnitude of H is solely dependent on r_0 (Fried's Seeing [2:429-431]). Fried's Seeing Parameter was developed to assist in modeling the atmospheric effects in imagery. A key ratio is in the exponent of Equation (3.2), where the ratio $\frac{r_0}{\lambda}$ describes the effect of the atmosphere in the image. In this equation λ is the mean wavelength of the light, ν is the spatial frequency and f is the effective focal length of the optical system. If the ratio is greater than 1, then the atmosphere will start to introduce blurring into the image. If it is less than 1, then the resolution of the image is unaffected by the atmosphere. [2:429-431]. Variables ν_x and ν_y represent the spatial frequencies in the x, y plane (camera detector plane), where the OTF is only relevant in the spatial frequency domain, and $\nu = \sqrt{\nu_x^2 + \nu_y^2}$.

$$H(\nu) = \exp\left(-\frac{1}{2} \left(\frac{r_0}{\lambda}\right)^2 \nu^2\right) \quad (3.2)$$

The least significant contribution in the blurring of the true intensity is due to the optics based OTF (H_o) given in Equation (3.3) [2:364]. H_o is the frequency domain representation of the system impulse response or PSF, $P(x, y)$ represents the pupil function, where x and y are spatial coordinates in units of meters. In this research the pupil function is defined at the lens of the telescope, where the pupil function directly determines the resulting optical transfer function [3:141]. The pupil function accounts for the effects caused by an aperture in a optical system [3:107]. Equation (3.3) is only true for the case of an incoherent light source. The blurring caused by H_o accounts for diffraction and other aberrations in the measured data. In this research diffraction is the only cause for any blur to the true intensity with respect to H_o . A diffraction pattern can be seen in Image C of Figure 3.1. This example shows how miniscule the diffraction based blurring is compared to the LEOTF blurring. The product of both OTFs gives the OTF for the system shown in Equation (3.3). H_{total} is the composite of both OTFs and is used for degrading all true intensity.

$$H_{total}(\nu) = H_o(\nu) \cdot H_a(\nu) \quad (3.3)$$

$$(3.4)$$

3.1.2 Noise Model

There are two types of noise to consider in this research and those are readout noise and photon counting noise. Both types of noise are present in photon counting cameras. Readout noise, also referred to as thermal noise is caused by imperfections in the analog to digital conversion process in a camera, and the injection of currents from other electronics in the circuitry. Readout noise variance can be measured by blocking light from entering the camera. The second type of noise considered is photon count noise, and is assumed to be the dominant source of noise in this research. It is safe to assume this if an avalanche photo-diode (APD) is used. The thermal noise becomes negligible due to the high amplification effects of this device. In this case the signal generated by each photon is amplified to a level above the readout noise level. Photon count noise is caused by incoherent light (i.e. sunlight) and can be modeled with Poisson statistics [12:16], [2:485]. The random arrival of photons counted by a camera detector is the consequence of photon count noise. Figure 3.2 shows an integration time window where there are eight expected photons arrivals along with the actual amount of nine arrivals. The irregular time of arrival of each photon contributes to the photon counting noise.

Photon counting noise is best described by use of the Poisson PMF [2:485]. Equations (3.5) and (3.6) show the general probability mass function for a Poisson random variable, and a Poisson PMF relevant in notation to this research [9:508]. In the general Poisson PMF equation λ is the random variable representing the actual number of occurrences. μ is the mean number of occurrences. $P(k)$ is the probability that the number of event occurrences is equal to k . Similarly, Equation (3.6) presents a two-dimensional case where the mean number of occurrences is μ_x , also known as the intensity, and the actual number of occurrences (photon counts at each pixel) is k_x .

$$P(k) = \frac{e^{-\mu} \mu^k}{k!} \quad (3.5)$$

$$P(k_x, k_y) = \frac{e^{-\mu_x} \mu_x^{k_x} e^{-\mu_y} \mu_y^{k_y}}{k_x! k_y!} \quad (3.6)$$

Equation (3.7) shows how the SNR is calculated for all scenarios. It also shows how one of the two variables in the denominator can be the dominant source of noise, if it is much greater than the other. The gain factor G_{APD} of the APD is shown in bold and only relevant if an APD is used. σ_e represents the thermal noise variance in electrons. S is the signal strength in photons with photon counting noise included in the signal [12:23-24]. Assume that σ_e is negligible compared to the noise included in S multiplied by G_{APD} . With this assumption the SNR ends up being the variance of the signal divided by the standard deviation of the signal, due to the properties of Poisson random variables.

$$\frac{S}{\sqrt{S + \sigma_e^2 G_{APD}^2}} \quad (3.7)$$

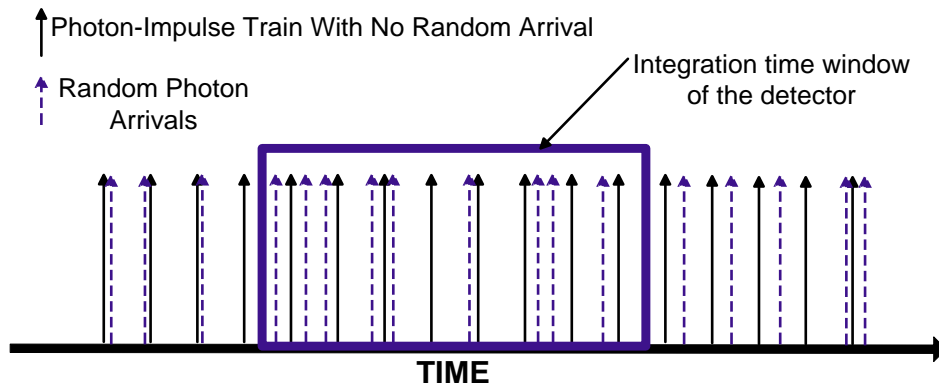


Figure 3.2: Random Photon Arrivals: There are expected to be 8 photon arrivals in the integration time window, but due to randomness of photon arrivals there actually 9 photon arrivals, and not at expected times.

3.1.3 Simulating Image Degradation

This section describes the simulation process for degrading the ideal true intensity to what is referred to as the measured data. An example of measured data can be seen in image E of Figure 3.1. Figure 3.3 displays an example diagram of a potential three channel polarimeter setup. Notice that each polarization analyzer is set in a particular direction and that there are three detectors for collecting three channels worth of “measured data.” The three polarization analyzers combined with three channels of measured data deem the necessary title 3 Channel Polarimeter.

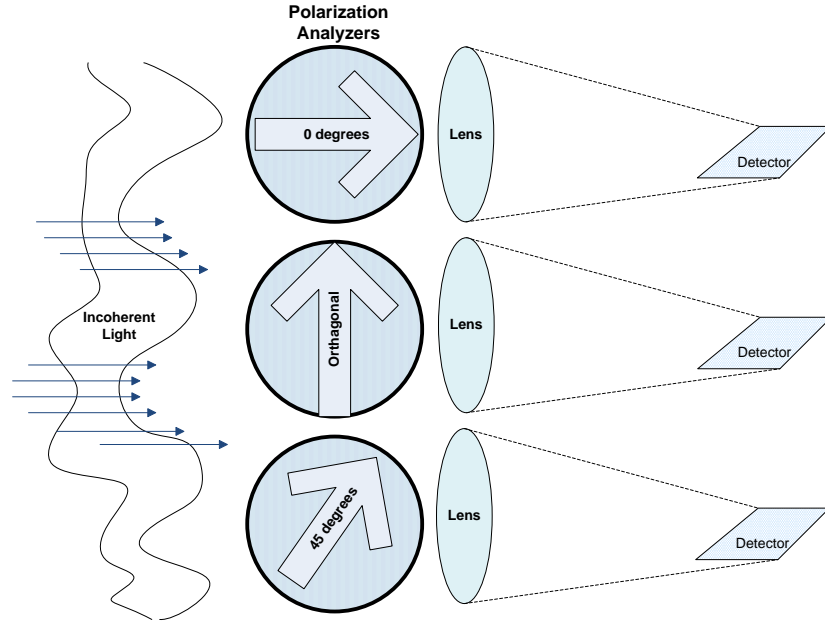


Figure 3.3: An example of the setup for a three channel polarimeter relevant to this research effort. There is an assumed incoherent light input to the optical system. There must be three polarization analyzers set as specified above, with three detectors to collect data from each analyzer.

Figure 3.4 below shows the logical flow of the data simulation process. The first three rhombuses represent data that is either created in the simulation program or uploaded for use in the simulation program. The true degree of polarization represents the degree to which light is polarized in the scene. Only certain parts of the object in observation will reflect polarized light. As the polarized light passes through the polarization analyzers a fraction of the light will be lost, unless it is in perfect alignment with one of the polarization analyzers.

The data represents the angle of polarization of each element in the polarization data. More importantly, is used to calculate three values, which corresponds to the three polarization attenuation factors. The variables , , and indicate the relative alignment of the polarized light with each channels' polarization analyzer.

The next three rectangles represent calculations for , , , LEOTF, and optics based OTF. Rectangle four initiates the process for degrading the true intensity. There are four sets of data that result from this step. First is $data_1$, which represents the unpolarized portion of light from the object being observed. The last three data sets correspond to the polarized light reflecting off the object in observation. Rectangle five represents the process for adding Poisson noise to the blurred data sets. It is most important here to understand that $data_1$ is used to

calculate the three unpolarized noise realizations along with the first polarized realization. Finally, the simulated measured data is calculated by adding each respective unpolarized component with its polarized partner. The three resulting data sets and are shown as an example in Figure 3.5.

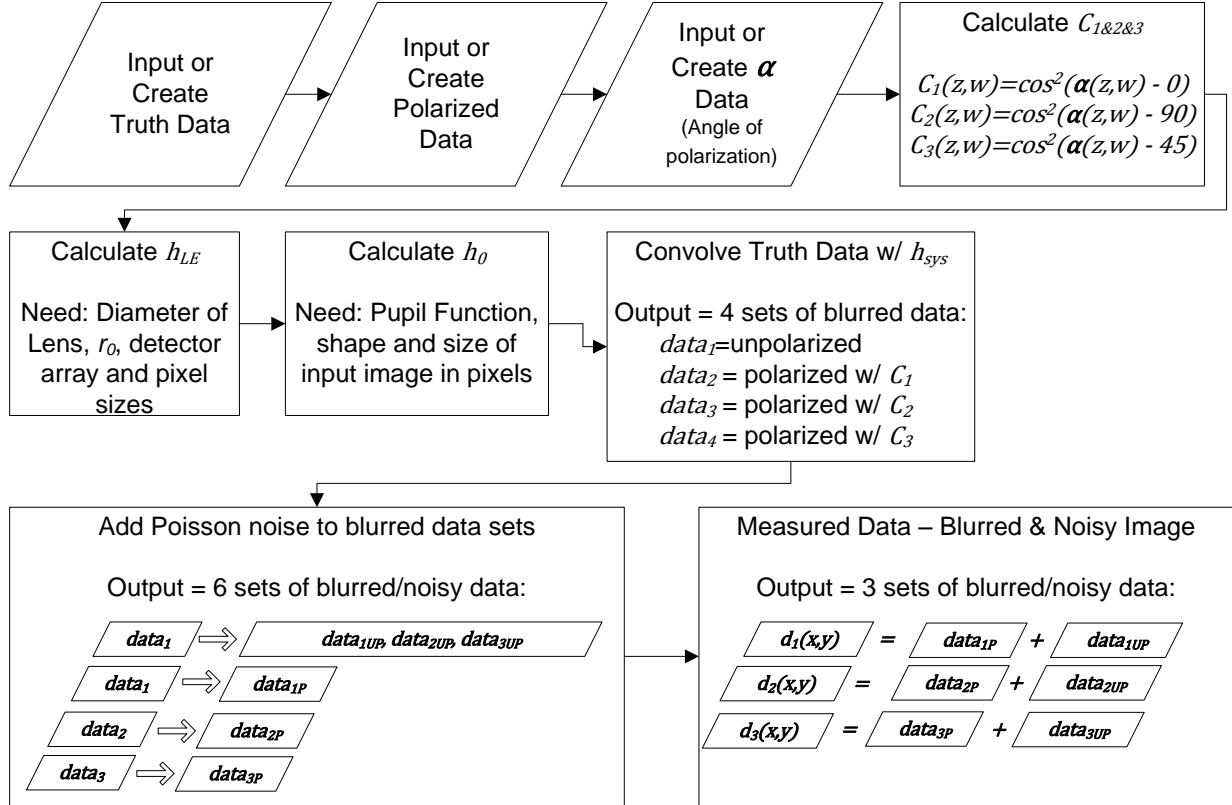


Figure 3.4: Logical flow of data degradation simulation process. Rhombuses represent creation or input of data to simulator. Rectangles represent calculations made in the simulation.

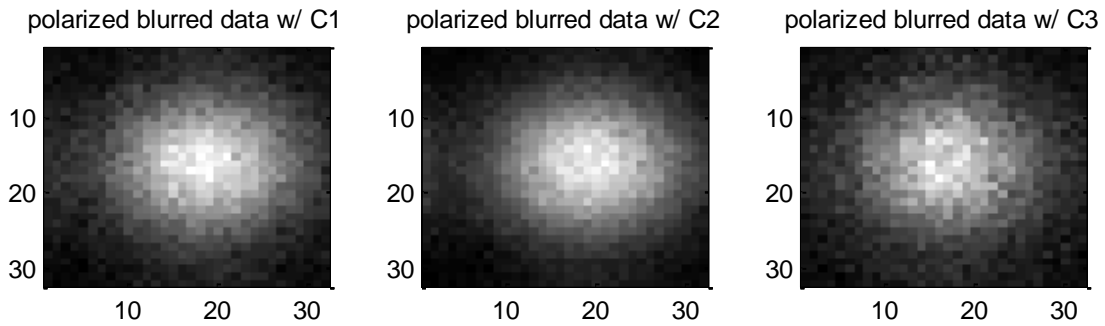


Figure 3.5: Examples of 2 binary stars degraded by Poisson modeled noise and blurring from . Left- . Middle- . Right- .

Equations (3.8-3.10) are the average value of and respectively. These terms can also be referred to as intensities, and . The intensity measurements look very similar to the measured data, but have no noise added. An example of an intensity image is shown in image B in Figure 3.1.

Equation (3.11) shows the mathematical relation between measured data and intensity. For further clarification of what the other variables in the Equations (3.8-3.10) are equivalent to refer to Table 3.1. These equations are a simple consequence of Malus' Law, which describes the intensity of the light passed by a polarization analyzer.) [4:332, 13:1067]. The discrete convolutions are approximations of the continuous case. These equations are also further explained in the derivation section (3.2.2).

(3.8)

—

(3.9)

—

(3.10)

—

(3.11)

Table 3.1: Equivalencies between Equations (3.8-3.10) and variables described in Figure 3.4

Equations 3.8-3.10	Figure 3.4	Notes
	data set	
	data set	Degree of Polarization
	True intensity	A.K.A object
	data set	Fourier Transform:

Next, an intuitive explanation of Equations (3.8-3.10) may be helpful in preparation for the deconvolution model (section 3.2), since it describes a derivation with these equations as a starting point. Remember that since the

optical system is linear and space invariant, the convolution of the input with a PSF can be generalized to the superposition integral as shown below (also in Equation (3.1)), but now the polarization analyzers must be accounted for in the convolution integral. The double sum of $\sum_{i,j} I_{ij} \delta_{ij}$ multiplied by the system PSF

is a convolution and it is this function that explains how objects in the observation plane are seen in the detector plane. Also, notice that P , C_1 , C_2 , and C_3 are just scalars on the range from (0,1). The next thing to notice is that the double sum is broken up into two components. The first component represents the unpolarized portion of light, while the second is the polarized portion. These equations show there is a combination of unpolarized light along with the potential for polarized light, depending on the object in observation. It is shown in Malus' Law that approximately half of the unpolarized light will be transmitted past the polarization analyzer [4:332].

3.2 Deconvolution Model

This section addresses the restoration process for transformation of measured data I_m to an estimated image that resembles the true intensity. The improvement in image sharpness is entirely a result of the measured data being run through a deconvolution algorithm. An extensive discussion of the mathematical derivation regarding the deconvolution algorithm takes place in this section after the simulation description is provided. The deconvolution algorithm works as displayed in Figure 3.6.

In simulation initial estimates for seven parameters must be created before the deconvolution can start. These seven parameters are shown at the top of Figure 3.6. These estimates constantly improve inside the deconvolution loop until a declared amount of iterations are exceeded. Although other criteria can be used to stop the algorithm they would require user input as does a maximum iterations criteria. Therefore in both cases there will be no algorithmic autonomy. This concept is explained later in Section 6.3. Definitions for the initial estimates are as follows:

1. r_0 = Fried's Seeing Parameter (same value used in r_0) (refer 3.1.1, and [2:429])
2. H_0 = Overall System Optical Transfer Function Estimate (refer to Equation (3.4))

3. = Object Estimate (arbitrarily set to 1)(refer to Table 3.1)
4. = Degree of Polarization Data (arbitrarily set to 1/2) (refer to 3.1.3, 3.2.2-Equation (3.32), and 3.2.3)
5. = Polarization Attenuation Factors (calculated from arbitrary set value) (refer to 3.1.3 & Table 3.2)
6. = Intensity estimates (calculated from exact value and arbitrary values for and) (refer to Equations (3.8-10))
7. = Conditional Expected Value of Complete Data Estimates (calculated from exact and measured data values, and arbitrary values for and) (refer to 3.2.2 Step 4 [13:4], [1])

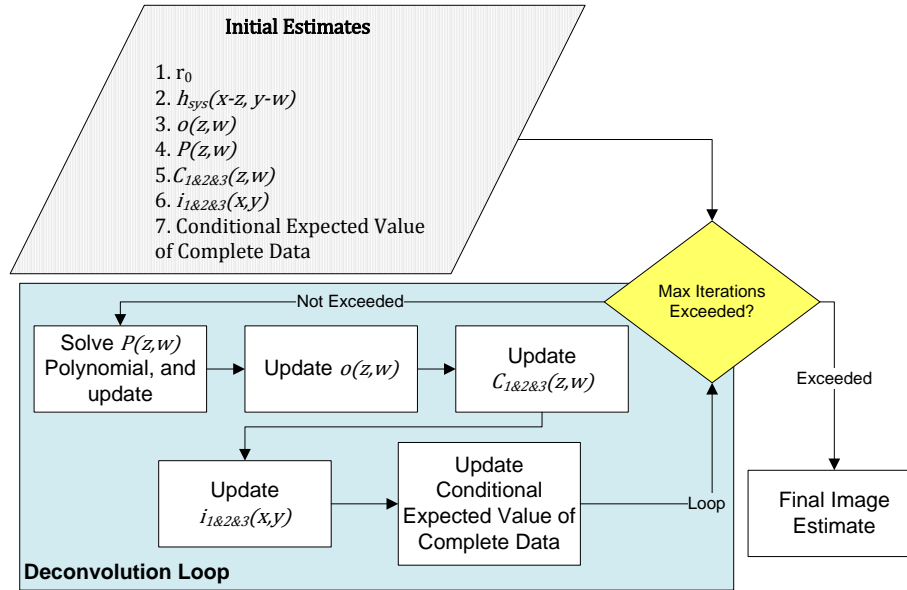


Figure 3.6: Deconvolution algorithm flow chart: The parallelogram consists of the seven necessary initial estimates. The large rectangle consists of all the calculations in the deconvolution loop. The diamond represents the decision to terminate to the deconvolution loop.

3.2.1 The Update Equations

Update equations are the key to this entire research effort. The results of these equations are responsible for the restoration process' level of success. The deconvolution loop in Figure 3.6 shows the parameters that are iteratively updated. Listed below in Equations (3.12 - 3.16) are the corresponding update equations (excluding intensity and conditional expected value of complete data, refer to Equations (3.8 - 3.10) and (3.25-28) respectively). Note that for the sake of brevity that all plane coordinates are not included for the the degree of polarization, the measured data and the complete data . Following this listing of equations is the math necessary to arrive at these update equations. Section 3.2.2 will briefly explain how each of these update equations are determined and what they are solving for.

(3.12)

(3.13)

(3.14)

(3.15)

(3.16)

3.2.2 Partial 3 Channel Polarimeter Derivation

A good portion of this research effort lies in the mathematical derivation for the three channel polarimeter restoration algorithm. This derivation relies on the results of years of research, as discussed in Chapter 2. This section explains the use of MAP estimation techniques in combination with the EM process. Essentially this derivation explains the mathematics necessary to take a blurred and noisy image and transform it into a sharper looking image.

The six steps listed below will briefly summarize the derivation for the three channel polarimeter restoration algorithm, while the full derivation is available in Appendix A. The first three steps below define the mathematical models for the types of data considered in this research, while the last three steps are the signature steps in the Expectation Maximization process.

Table 3.2: Definitions of the variables for the 3 Channel Polarimeter Derivation.

Detector Plane coordinates:	
Observation Plane coordinates:	
Incomplete Data (measured):	
Complete Data Unpolarized Component (mythical):	
Complete Data CH 1 Polarized Component (mythical)	
Complete Data CH 2 Polarized Component (mythical)	
Complete Data CH 3 Polarized Component (mythical)	
True Intensity (object):	
Simulated Image (intensity):	
System Point Spread Function:	
Pixels, or image size:	
True Degree of Polarization:	
Polarization Attenuation Factors:	$1/2$ —

Step 1: Obtain a Statistical Model for the Incomplete Data (Measured Data)

Recall Equations (3.8-10) from section 3.1.3 and the double sums over the values x and y , which are the coordinates in the observation plane (outer-space). Notice that the intensities have coordinates in the u plane, also known as the detector plane (camera detector). These three equations mathematically explain the occurrence of a convolution. Also recall that the measured data (equivalent to incomplete data) is $I_m(x, y)$. It is called incomplete data because it is not a direct measurement of an object in observation, whereas the complete data represents a direct measurement of an object in observation (refer step 2). The average value of the incomplete data shown below and in Equations (3.8-3.10) builds upon Schulz's model by accounting for polarization effects, thus adding the true degree of polarization and polarization attenuation factors. [13: 1067]

—

—

—

Step 2: Invent a Set of Complete Data (Mythical)

The complete data \mathbf{I}_c is a mathematical construct designed to be a direct measurement of the image without the convolution operation, therefore it represents the object in observation before its light passes through the atmosphere. The convolution function is the mathematical reason for the occurrence of blurring. Equations (3.17-3.19) are broken up into two parts. The first part is a double sum of the unpolarized component of the complete data, and the second part is the double sum of the polarized component of the first channel of data. The complete data are chosen to be independent Poisson distributed random variables, which means that the incomplete data will also be a Poisson distributed random variable. This is due to the statistical property that the summation of Poisson random variables is a Poisson random variable. [13: 1067] Note that the mean of unpolarized complete data are mathematically equivalent so,

(3.17)

(3.18)

(3.19)

Step 3: Select a Statistical Model for the Complete Data

The main goal in selecting a statistical model is ensuring statistical consistency between the incomplete and complete data. As stated in the last step the complete data in this derivation was chosen to be modeled as Poisson data, because the sum of Poisson random variables is a Poisson random variable [13: 1067, EQN 15]. Equations (3.20-3.23) show the mean of the complete data sets.

$$\text{Where } \mu_{\text{unpolarized}} = \dots \quad (3.20)$$

$$\dots \quad (3.21)$$

$$\dots \quad (3.22)$$

$$\dots \quad (3.23)$$

Step 4: Formulate the Complete Data Log-Likelihood

The complete data log-likelihood function is formulated assuming that the complete data are statistically independent. Equation (3.24) shows the log of the joint probability for all of the complete data. Once again, this equation resembles Schulz's log-likelihood function, except for the notational differences, additional channels of data, and polarized data (). [13: 1067-Equation 17]

$$\dots \quad (3.24)$$

Notice the addition of polarization prior to the end of Equation (3.24). The main reason for adding this is to constrain the values of polarization to be between 0 and 1, which is “prior” known information [7:310 & 350]. The PDF chosen to model this prior is a Super Gaussian, . This PDF was chosen because it approximates a uniform PDF on (0,1) for high values of n. A uniform PDF has to be approximated because of discontinuities in its derivative [6:23].

Step 5: Expectation Step

The conditional expected value of the complete data log likelihood must be computed in order to formulate the EM algorithm. The conditional expectations of each piece of complete data are conditioned on the incomplete data and the estimates of , , , and . They are shown below in Equations (3.25-3.28) and computed using results from Shepp and Vardi [14:115 & 119], [13:1067, EQN 26]. The resulting conditional expectations will differ from the results derived by Shepp and Vardi, and also from Schulz’s results for conditional expectations [14], [13]. This is strictly due to the fact that this research is using three channels of polarimetric data.

$$\text{_____} \tag{3.25}$$

$$\text{_____} \tag{3.26}$$

$$\text{_____} \tag{3.27}$$

$$\text{_____} \tag{3.28}$$

The expected value of the complete data log likelihood is added to the natural logarithm of the prior to yield the Q function shown below:

$$\tag{3.29}$$

Step 6: Maximize the Expected Value

This step requires the most algebraic manipulation, since the derivative of _____ with respect to _____, _____, _____, and _____ must be calculated, and then set equal to zero. For the sake of brevity only the results of each derivative will be shown, along with the four conditional expectations. A more detailed derivation is shown in Appendix A.

$$\text{_____} \tag{3.30}$$

$$\text{_____} \tag{3.31}$$

$$\tag{3.32}$$

The most important operation in the deconvolution loop is the estimation of \hat{O} . This is accomplished by solving for the roots in Equation (3.32). Once \hat{O} has been estimated the object, intensities, \hat{I} and complete data expectations can be estimated (refer Figure 3.6).

3.2.3 Point Source Pixel Spacing

One last concept needs explanation before the simulation results can be discussed and this is how the ratio of the lens diameter D determines the dual point source pixel spacing in the detector plane (refer to Figure 3.7 and Equation (3.33)). If an observer is viewing two stars in space that have an angular separation θ radians through a D meter diameter lens, then the resulting spacing in the detector plane will be Δx meters. For example, assume simulation parameters equal to: $\theta = 0.001$ radians, $D = 1$ meter, resulting in $\Delta x = 0.001$ meters. If the lens diameter changes to $D = 2$ meters then Δx must change accordingly to $\Delta x = 0.0005$ meters. Assuming that the camera pixel detector size = 0.001 meters, then a $D = 1$ meter lens would have $\Delta x = 0.001$ meter spacing, whereas the $D = 2$ meter lens would have $\Delta x = 0.0005$ meter spacing. To ensure consistency in all simulations this fact needs to be considered, because the angular separation of the stars will not change, but the simulation parameter D will change to 2 or 0.5 , resulting in different values for pixel spacing. These two lens sizes were chosen because they are the actual sizes of telescope lenses at the Maui Space Surveillance Site (MSSS) [16]. Use of these lens sizes ensures more meaningful results for Maui Air Force Research Labs, the sponsor of this research.

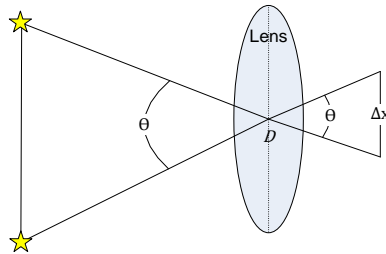


Figure 3.7: θ is the angular separation of 2 point sources in space. D is the diameter of the lens of a telescope and Δx is the distance or pixel separation in the detector plane. The angular separation does not change, but a change in D will determine a change in Δx .

$$\Delta x = D \theta \quad (3.33)$$

Another topic related to the point source pixel spacing is proper sampling of data. To assure proper Nyquist sampling criteria consider Equations (3.34) and (3.35) [12:57]. Assume the following parameters for a given scenario:

Also, assume that focal length is adjustable, which in the case of MSSS telescopes is true. Based off of Equation (3.35) these parameters determine to ensure proper sampling in space. If , then —, giving a Nyquist sampling frequency of —.

$$\text{---} \quad (3.34)$$

$$\text{---} \quad (3.35)$$

4. Simulation Results

Simulation results are important for learning the ideal performance of the three channel polarimeter. It is possible to accurately measure performance because the final object estimate can always be compared to the true intensity. This comparison allows for a total squared error (TSE) comparison and most importantly a resolution comparison. Resolution comparisons are important, because the goal of this research is to “see” whether the three channel approach can improve upon the two channel approach.

This section analyzes the simulation results from two types of simulations. The first type of simulation is a dual binary star simulation. In space imaging a dual point source image could be the result of viewing two stars close to each other in an angular separation sense. The second type of simulation is executed with an actual satellite image.

4.1 Dual Point Source

The dual point source simulation results are shown in Figures 4.1 and 4.2 below. Both figures are composed of six images. The top left image in Figures 4.1 and 4.2 are the true intensity. It represents two point sources with pixel spacing equal to nine pixels for the lens simulation and twelve pixels for the case. The degree of polarization data is not shown, but in all dual point source cases the left point was fully polarized and the right point was half polarized. The top right image in both figures is the final object estimate for the two channel case. All other images in both figures are final estimates for the three channels at different values. The corresponding TSEs are displayed in a table below each representative figure. The TSE was calculated using Equation (4.1) below. The comparisons between the two and three channel algorithms are consistent in that the total intensity estimated in each image is conserved. This ensured that the total number of photons in the true intensity and final object estimate are the same.

(4.1)

The figure captions also define some other very important simulation parameters. First is the lens size in centimeters. Second is the seeing parameter r_0 in centimeters. The third value requires a little explanation, since it differs for the three and two channel results. To ensure consistency in comparisons the signal strengths must be

relatively equal. This means that if the true intensity's two point sources are represented by 200,000 photon counts in each white pixel in the two channel polarimeter, the three channel must have 2/3 the amount of photons, because it splits the light signal into three channels, versus two channels. The fourth value is the point source pixel spacing. Fifth is the number of iterations used in the deconvolution. The sixth number is the angle of polarization in the observation plane. This angle directly impacts the three polarization attenuation factors (refer to the first calculation rectangle in Figure 3.4 to see mathematical correlation). Lastly, the numbers along the x-axis and y-axis show the size of the image. Simulations for the lens used an image size of 32x32 pixels. Simulations for the lens used 46x46 pixel images.

4.1.1: 160 cm Lens Results

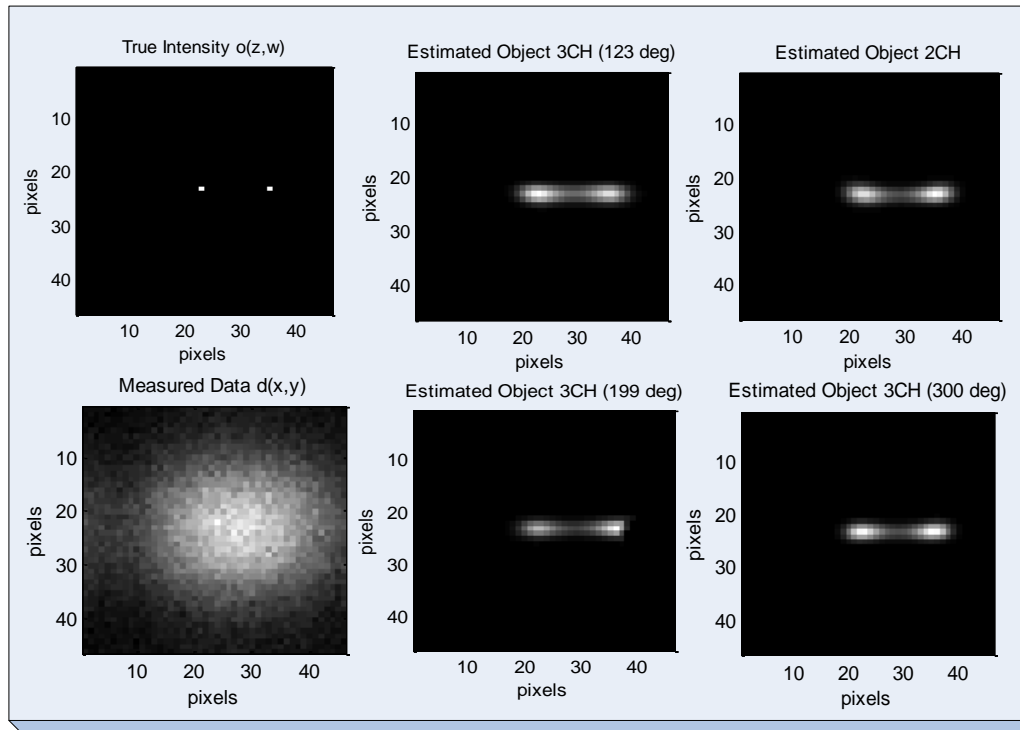


Fig. 4.1: Results for: Lens = 160 cm; $r_0 = 15$ cm; Signal Strength = 134k/200k photoelectrons; Point Source Spacing = 12 pixels; Iterations = 6000. Note: all Final Estimated Objects are for 3 CH results, except top right image. The TSE for the 2 CH is nearly double the 3 CH estimates and is shown in Table 4.1. The visual reproduction of the true intensity is close to the same for all deconvolutions.

Table 4.1: TSE values for 160 cm lens results

	TSE Value
2 CH	$7.32E^{10}$
3 CH ($\alpha=123$)	$3.31E^{10}$
3 CH ($\alpha=199$)	$3.25E^{10}$
3 CH ($\alpha=300$)	$3.26E^{10}$

4.1.2: 120 cm Lens Results

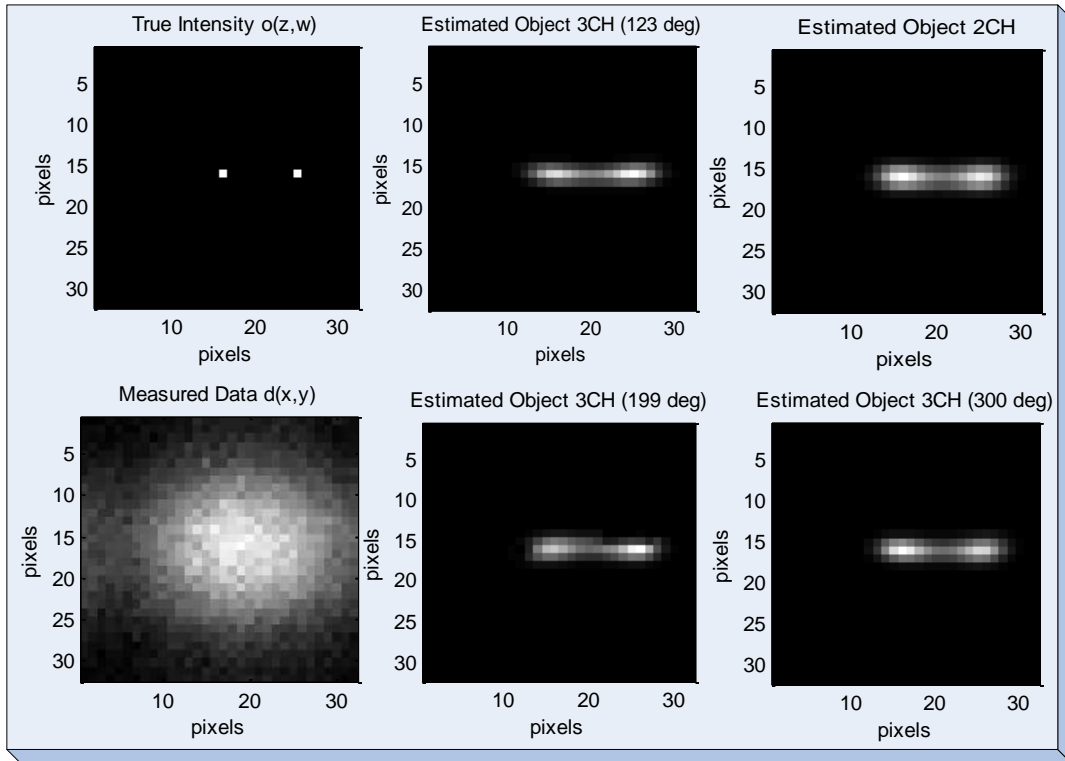


Fig. 4.2: Results for: Lens = 120 cm; $r_0 = 15$ cm; Signal Strength = 134k/200k photoelectrons; Point Source Spacing = 9 pixels; Iterations = 6000. Note: all Final Estimated Objects are for 3 CH results at differing α values, except top right image. The TSE for the 2 CH is nearly double the 3 CH estimates and is shown in Table 4.2. Visually the 3 CH is better.

Table 4.2: TSE values for 120 cm lens results

	TSE Value
2 CH	$7.13E^{10}$
3 CH ($\alpha=123$)	$3.12E^{10}$
3 CH ($\alpha=199$)	$3.13E^{10}$
3 CH ($\alpha=300$)	$3.15E^{10}$

Visually, it is difficult to discriminate if the three channel algorithm provides a closer reproduction of the true intensity, which effectively demonstrates better resolution. The TSE values in Table 4.2 provide a numerical metric for comparing performance showing the three channel algorithm's superiority.

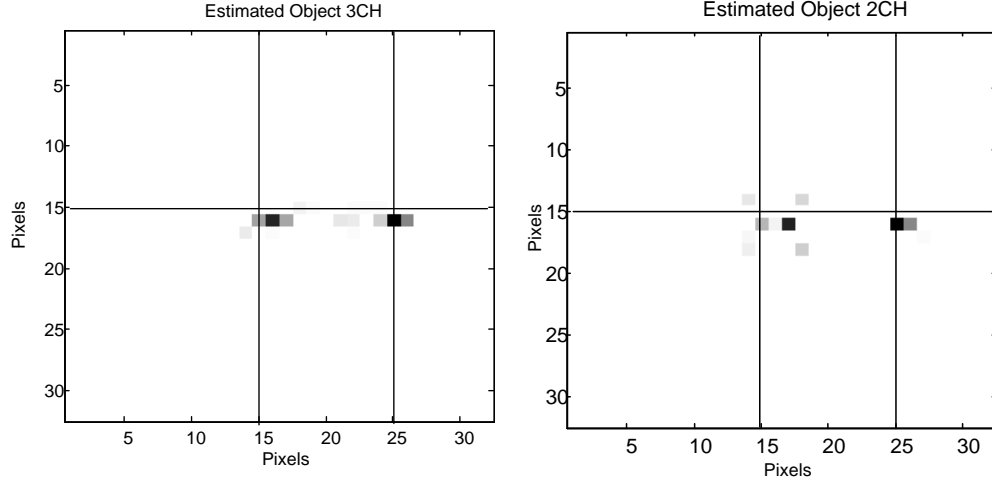


Fig. 4.3: Results for: Lens = 120 cm; $r_0 = 15$ cm; Signal Strength = 134k/200k photoelectrons; Point Source Spacing = 9 pixels; Iterations = 448k/500k. Note: the color inversion from other images and that the 3CH performs better because both of the darkest pixels are exactly where they are supposed to be, which is pixel (16, 16) and (25, 16). The TSE values are $1.22E^{10}$ for the 3 CH and $1.62E^{10}$ for the 2 CH.

The best way to actually determine which algorithm works better is to analyze the TSE values. In all simulation cases at 6000 iterations the TSE values for the two channel are more than double that of the three channel results. Figure 4.3 shows an exception to this statement. In this figure it is evident that the three channel algorithm outperforms in visual reconstruction of the true intensity, because the darkest spots in the image are actually located in correct pixel locations with respect to the true intensity. These pixel locations are $(16, 16)$ and $(25, 16)$, hence the separation for the r_0 lens. It is also evident that the TSE value is lower, but only by 25% this time. The TSE value is important in this research because it provides quantification for both algorithms' performances.

4.2 Satellite Image

The satellite image simulation provides a better sense of both algorithms' performance on a more complex image. There are three given sets of data needed for the satellite image simulation. Only the first two sets of given data are shown in the left and middle of Figure 4.4, while the third data set (angles of polarization data) is not shown because it looks identical to the polarized data image. The left image is the true intensity, which is the ideal satellite image. The second image is the polarization data, which represents the parts of the satellite reflecting polarized light. The right image is the measured data, which is a blurred version of the truth data due to the simulated system PSF. Figure 4.5 shows the images produced by the two and three channel algorithms.

4.2.1: 160 cm Lens Results

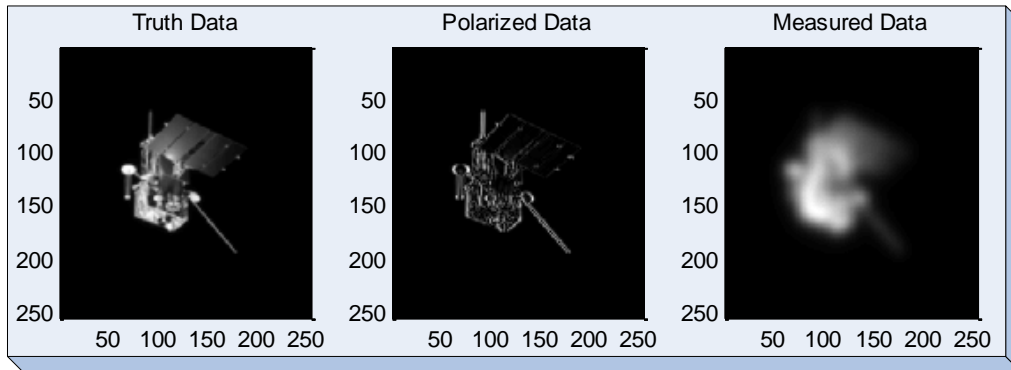


Figure 4.4: Left: True intensity. Middle: Polarized data. Right: Measured data (160 cm lens, $r_0=22$ cm)

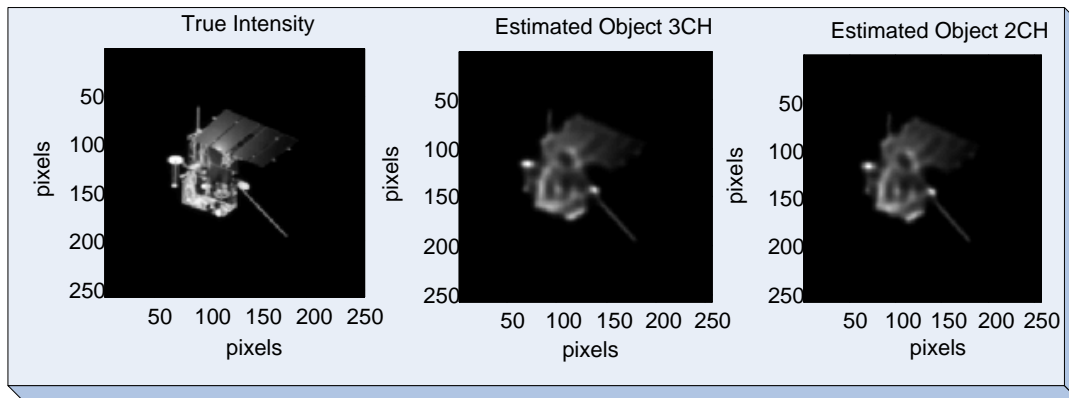


Figure 4.5: Left: True intensity. Middle: 3 channel estimate with 4000 iterations. Right: 2 channel estimate with 4000 iterations. $r_0 = 22$ cm. The TSE value of the 3CH is $2.58E^{10}$, which is approximately 60% the value of the 2 CH TSE at $4.25E^{10}$. This is consistent with the dual point source simulations. The visual results of the true intensity reconstruction are near identical.

4.2.2: 120 cm Lens Results

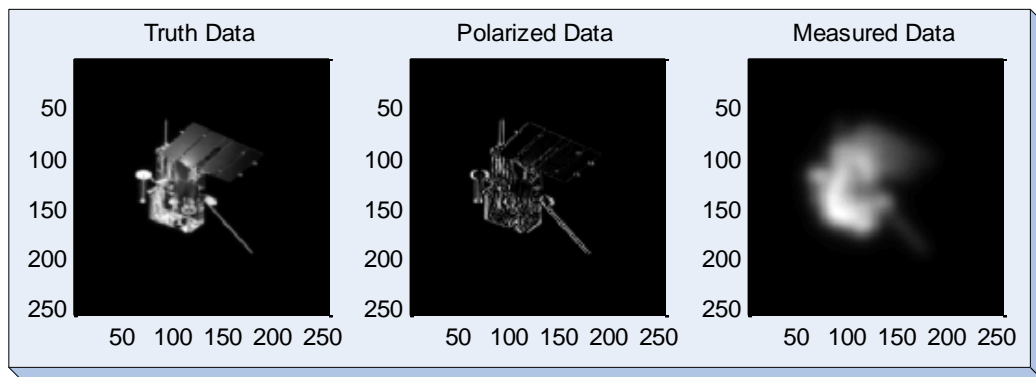


Figure 4.6: Left: True intensity. Middle: Polarized data. Right: Measured data (120 cm lens blur, $r_0 = 15$ cm, that is why the measured data appears more blurry than the measured data for the 160 cm, $r_0 = 22$ cm.)

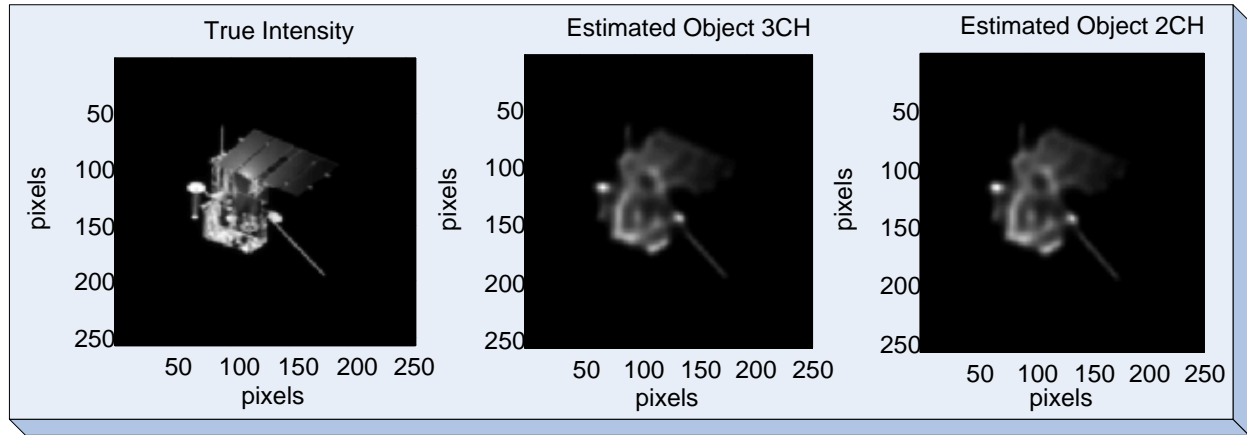


Figure 4.7: Left: True intensity. Middle: 3 CH estimate with 4000 iterations. Right: 2 CH estimate with 4000 iterations. $r_0 = 15$ cm. The TSE value of the 3CH is $2.94E^{10}$, which is approximately 60% the value of the 2 CH TSE at $4.79E^{10}$. This is consistent with the dual point source simulations. The visual results of the true intensity reconstruction are near identical.

When viewing the results for the satellite deconvolution in Figure 4.7 there is no visible difference between the results of both algorithms. Even if larger sized images were provided there would be no visible difference. Even though the three channel polarimeter will provide slightly higher resolution in the deconvolution, it is not significant enough to make a visible difference in the satellite image deconvolutions. In this case the TSE for the three channel algorithm was not quite half the value of the two channel algorithm, but closer to 60% of the two channel value.

Remember that the dual point source simulations for a lens used a nine pixel separation, and twelve for the lens. Figure 4.8 shows how poorly both algorithms perform when the pixel separation is significantly decreased. Now, consider the satellite image, where it would be necessary to be able to deconvolve point sources with separations as little as two or three pixels to get a much better estimate of the true intensity. If both algorithms can barely deconvolve at nine pixels of separation, then how could they ever deconvolve details of the satellite image, which have details with two or three pixels worth of separation. In conclusion the algorithms do have slight differences in performance, but not enough difference to visually distinguish between both deconvolutions. The only way to distinguish between the three and two channel results is to compare TSEs and binary star results. The TSE for the two channel is still close to double the value of the three channel result. The error is evenly distributed through the illuminated portion of the images.

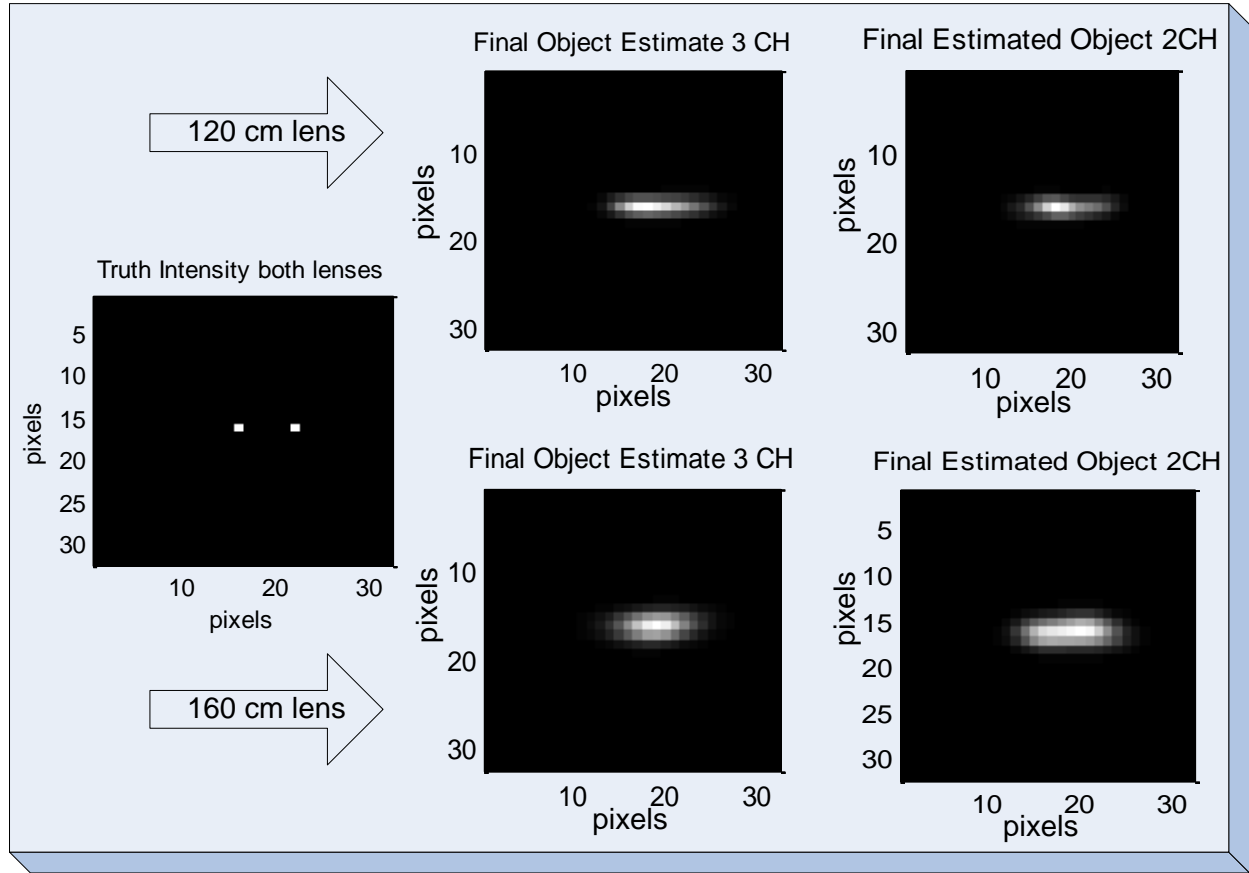


Figure 4.8: Comparison of the 3 and 2 channel algorithm at 6 pixel separation shows poor performance by both. The top images are the results for a 120 cm lens simulation with $r_0=15$ cm. The bottom images are the results for a 160 cm lens simulation with $r_0=15$ cm.

5. Laboratory Imagery Results

5.1 Laboratory Setup

Analysis of laboratory imagery with the three channel algorithm takes this research one step further in proving its success and efficacy. However, the given imagery and results in this section can only model actual data gathered from a telescope. The laboratory images were gathered as shown in Figure 5.1. The light source for this experiment was a light emitting diode (LED). Light passes through the multi-sized triple slit pattern to the lens, where it is then focused through a polarization analyzer to the CCD camera.

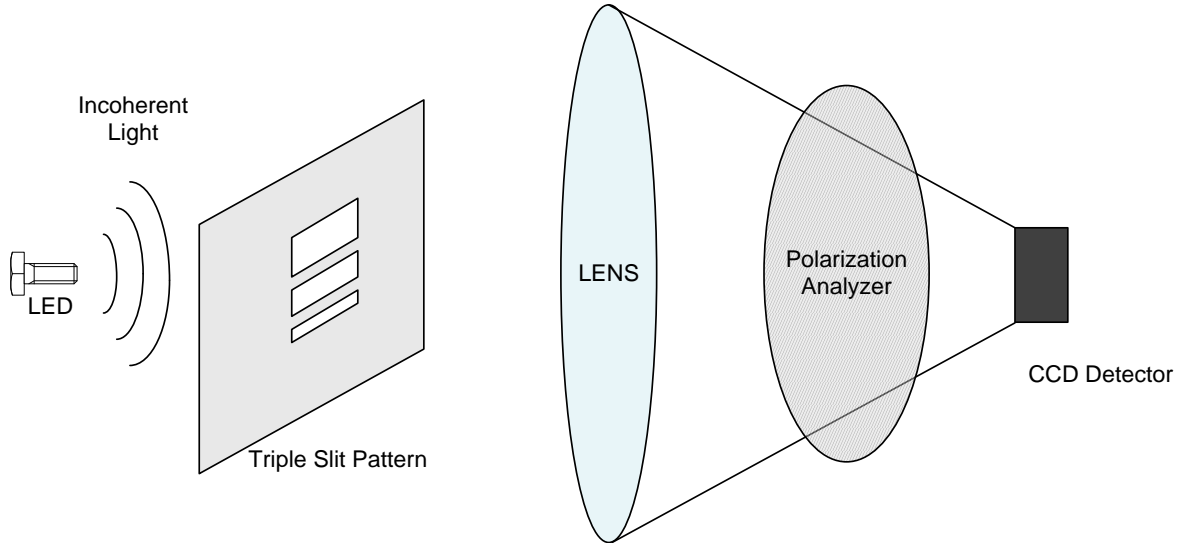


Figure 5.1: Laboratory Experiment Setup: light source is an LED. Light passes through the multi-sized triple slit pattern to the lens, where it is focused down to the CCD camera through a polarization analyzer.

5.2 Laboratory Image Blur and Noise

The blurring that would be caused by atmospheric turbulence in astronomical images is accounted for in the lab images by defocusing the camera, so the laboratory images appear blurred (refer to Figure 5.2). This is a reasonable way to simulate the atmospheric turbulence assuming the severity of defocus is actually comparable to the severity of blurring caused by the atmosphere. One way to assure a reasonable amount of blurring due to defocus is to compare the OTF of the lab data to the simulated OTF as explained in section 3.1.1. This is a reasonable comparison because the OTF can be thought of as a low pass filter. If the filter's (OTFs) can be matched to each

other by matching cutoff frequencies and overall shape of the curve, then it is reasonable to assume that they will have the same effect on any given truth data.

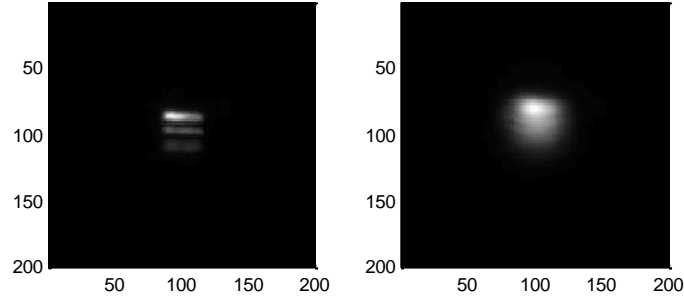


Figure 5.2: Left: in focus image (True Intensity) of triple slit taken from CCD camera. Right: out of focus image of triple slit pattern to simulate blur in an image caused by atmospheric turbulence. Note: the polarization analyzer was removed for this picture.

The lab data PSF was created from the standard Richardson Lucy deconvolution algorithm given in Equation (5.1) [11], [13:1066]. However, instead of estimating new values of the object using old estimates of the object () (where is the Fourier transform of the measured data, is the Fourier transform of intensity, and is the complex conjugate of the OTF), now the PSF is going to be estimated in a similar way as the object was. This is shown in Equation (5.2), where the symbol represents the correlation function.

$$\text{---} \quad (5.1)$$

$$\text{---} \quad (5.2)$$

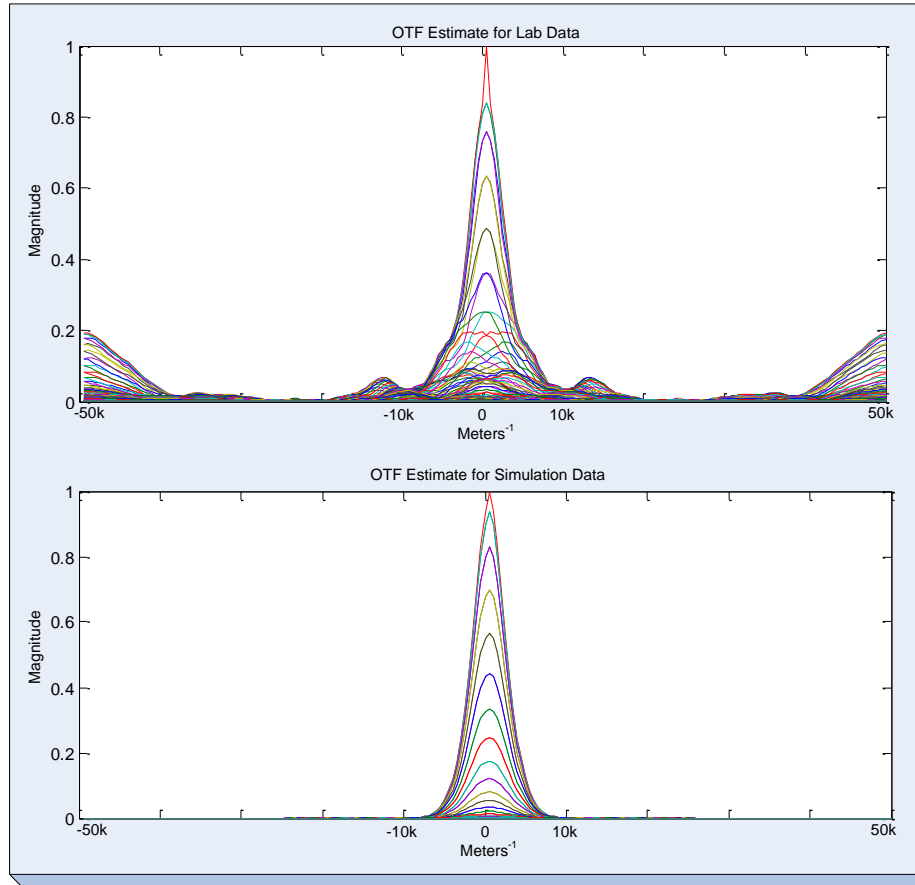


Figure 5.3: A comparison of Lab generated OTF vs. Simulated data OTF (). The plots are nearly identical if the side lobes of the top plot are ignored, which means that these OTF's are a match leading to the same effect on any given truth data. Cutoff frequencies for both plots are approximately -10k and 10k m^{-1} .

The OTF of the lab data is the Fourier transform of $I(x)$ after the algorithm in Equation (5.2) has converged. A plot of this OTF versus a plot of $I(x)$ from section 3.1.1 is shown in Figure 5.3. $I(x)$ was generated using a lens diameter of 10 mm and an f of 100 mm , which are the same parameters used in sections 4.1.2 and 4.2.2. The bell shapes of the plots are a very good match to one another and they almost completely attenuate all spatial frequencies before and after the values of -10 k m^{-1} and 10 k m^{-1} respectively. This is excluding the fact that the lab data OTF has side lobes, which is something the ideal simulated data will never deal with. The key to assuring that these two plots are reasonably comparable is to ensure that the truth data image in simulation is the same as the images measured for the lab data.

The dominant source of noise is still be assumed to be photon count noise as it was for the simulations, because the thermal noise is insignificant when compared to the photon count noise. Since the PSF was calculated using a Richardson Lucy algorithm, it must be assumed that the noise is modeled with Poisson statistics, because the

derivation to arrive at Equation (5.1) requires a Poisson model for the probability of a photon arrival (refer to Equation (3.6)) (Derivation Available in Appendix B).

5.3 Laboratory Results

The results in Figure 5.4 show an overwhelmingly impressive performance by the three channel compared to the two channel algorithm. There are three different results shown for the two channel algorithm at the bottom of the figure. Each two channel result is based off of a deconvolution with the unpolarized channel of measured data along with either the 0° , 45° , or 90° data. The two channel algorithm seemed to have some issues in noise amplification, which explains the white spots all over the images. The suspected reason for the three channel algorithms' success is mostly due to the polarization diversity provided by three channels worth of polarized data, compared to the two channels' need for an unpolarized and arbitrarily polarized channel of data. This concept and limitation is further explained in section 6.4.

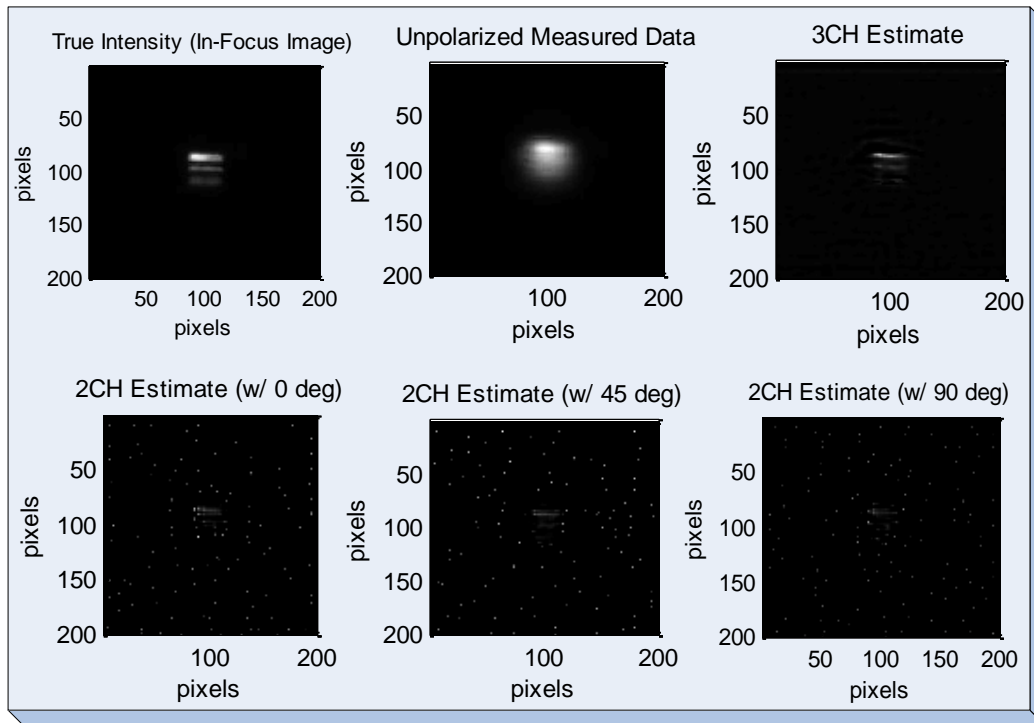


Figure 5.4: Lab results at 1000 iterations: Top left: in focus image (True Intensity) of triple slit taken from CCD camera. Top middle: Unpolarized measured data. Top Right: 3CH deconvolution estimate. Bottom Left: 2CH deconvolution estimate with 0° data and unpolarized data. Bottom middle: 2CH estimate with 45° data. Bottom right: 2CH estimate with 90° data.

6. Limitations

6.1: ratio

The most detrimental limitation in this research is the reality that the ratio $\frac{D}{\lambda}$ will always determine the severity of blurring. This fact is inescapable. Recall Equation (3.2), where the LEOTF is described, and Equation (3.39), where the maximum spatial frequency is given. Remember the $\frac{D}{\lambda}$ in the exponent of Equation (3.2) and notice how the lens diameter D in the equation below can be substituted in for the numerator. This proves that the ratio of lens diameter to the seeing parameter λ determines level of blur in an image.

6.2: No Blind Deconvolution:

A second limitation is that the three channel algorithm is not capable of performing blind deconvolution. It was originally in the scope of this research effort to include blind deconvolution capability in the three channel algorithm. In simulation the estimated λ equaled the true λ value. Therefore, the system OTF was always predicted perfectly. For deconvolution of the laboratory data the PSF was calculated by use of the Richardson Lucy deconvolution algorithm. The impact of not being able to do blind deconvolution is not too severe, since in the case of advanced laboratories the seeing parameter can be measured separately.

6.3: Lack of Algorithmic Autonomy (no stopping criteria)

A potential source of contention in this research is the lack of a stopping criterion for the deconvolution algorithm. The previous two channel research by Capt James included the use of a stopping criterion [6]. The criterion was based off of a total squared error comparison between the incomplete data and the estimated intensity per iteration versus the variance of the corresponding incomplete data [6:29]. The theory behind the stopping criterion is explained in his research and the comparison equation is given below as:

(6.1)

The main purposes of the criterion were to add autonomy to the deconvolution algorithm, and most of all to avert over-iteration of the estimated object. The issue of over-iteration is of no consequence in this research and is proven below, while the lack of autonomy is a potential limitation, but not of severe consequence. It is shown by simulation (Figure 6.2) that the total squared error of the final object estimate versus the true intensity continuously trends downward, and that the likelihood of the object being estimated as the true intensity always increases (Figure 6.1). Theoretically the likelihood should always increase. There are slight spikes in the TSE plot showing that the TSE does not actually always go down, even though it trends downward. This does not mean that the algorithm does not work correctly, but is more likely a numerical issue in MATLAB (simulation program). Numerical issues like this can be attributed to round off errors in floating point numbers, or some of the logic added to the deconvolution algorithm to avoid dividing by zero.

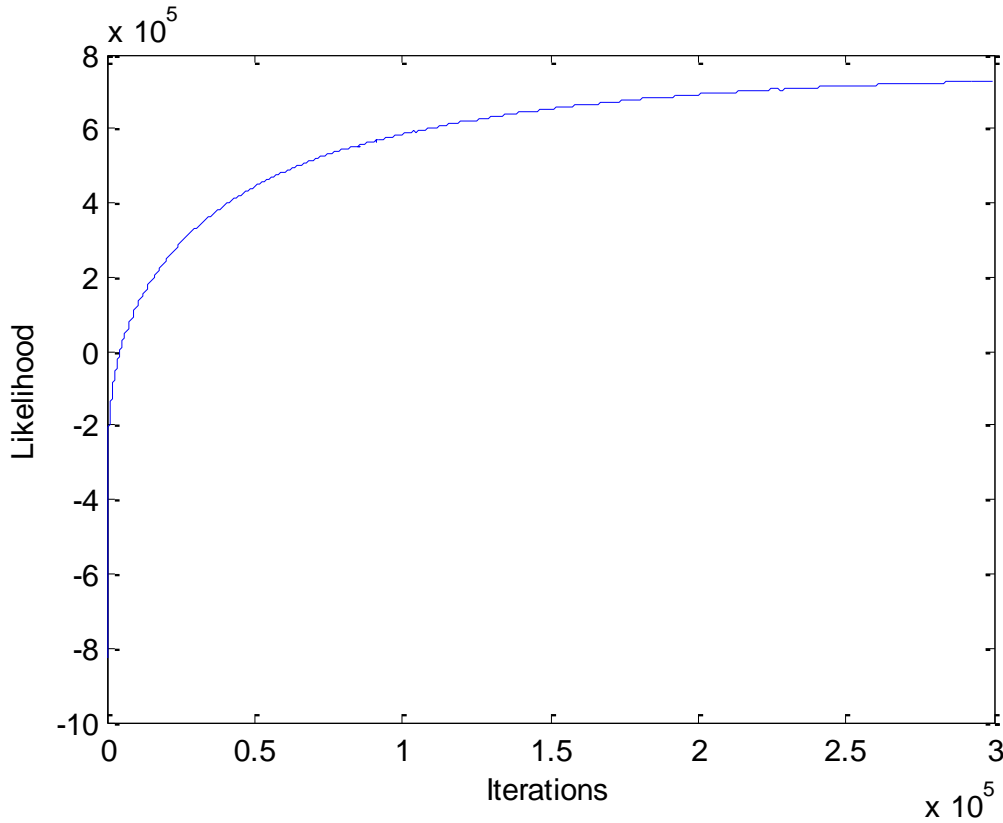


Figure 6.1: Likelihood of 3CH estimated object converging towards true intensity at 300k iterations. This simulation was run with 120cm diameter lens and an $r_0 = 15\text{cm}$.

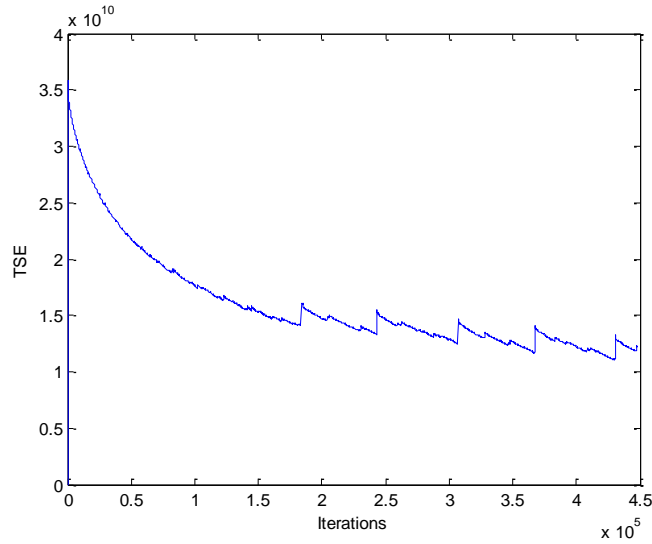


Figure 6.2: Total Squared Error of 3CH estimated object versus true intensity at 448k iterations. This simulation was run with 120cm diameter lens and an $r_0 = 15\text{cm}$.

6.4: Diversity of Multi-Channel Data due to Polarization

The more diversity there is in a set of data, whether it is two or three channels worth of data will give a better deconvolution with both the two and three channel algorithms. In the case of the laboratory data the three channel significantly outperforms the two channel because of this fact. Figure 6.3 below shows that the 45° data is significantly affected by the setting of the polarization analyzer. This channel of data is completely missing the lowest bar worth of light, because it was blocked by the polarization analyzer at a 45° setting. The two channel algorithm did not perform nearly as well, because it required an unpolarized channel of data along with a polarized channel (0° used in comparison in Chapter 5), where there wasn't enough diversity to allow for a better deconvolution. If there were less diversity in the three sets of data, then the potential for success in deconvolution is significantly hampered. This is one significant downfall for multi-channel polarimeter based deconvolution algorithms.

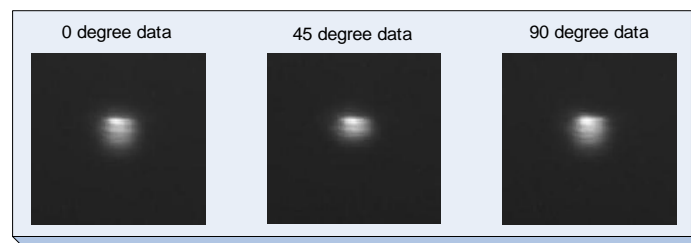


Figure 6.3: 3 channels worth of laboratory data. Shows that the polarization analyzer set at 45° impacts the triple bar image by blocking light from the 3rd bar (or lowest bar).

7. Conclusions

Atmospheric turbulence will always have a degenerative effect on imagery, which is dependent on the earth's atmosphere as a medium for light to travel. Polarimetry in conjunction with deconvolution has proven to be an effective method for mitigating these negative atmospheric effects. The reason polarimetry is so effective is that it creates the potential for diversity in imagery, which is advantageous for the three channel algorithm. More importantly, it shows that the three channel algorithm always outperforms the two channel, even though in some cases resulting imagery may appear to be the same. Simulations showed that TSE estimates were always significantly better, while visual comparisons for the three channel were always better or the same as the two channel. Conversely, in the laboratory comparison the three channel provided a far superior reconstruction of the true image, while the two channel had apparent issues with noise amplification.

Though there are some limitations with the three channel algorithm as described in Chapter 6, there is definite potential for future research to be done in continuation with the developed algorithm. This research effort only consists of results from a laboratory and simulation environment, so the obvious next step is to use the three channel algorithm with actual telescope imagery. There also needs to be more research done in the area of developing effective stopping criteria for the deconvolution algorithm, since the only stopping criteria used is a declaration of maximum iterations. Once this is successfully completed the algorithm can start to be used in an operational environment to actually assist the DoD in space situational awareness. There is also potential for the three channel algorithm to be combined with concepts of other research, such as described in Milo Hyde's IEEE article, "Material Classification of an Unknown Object Using Turbulence-Degraded Polarimetric Imagery." If this research is continued and completed it may provide significant capability to the DoD, and as a result better national security for our wonderful United States of America.

Appendix A: 3 Channel Polarimetric Data Deconvolution Algorithm Derivation

Detector Plane coordinates:	x,y
Observation Plane coordinates:	z,w
Incomplete data (measured):	$d_1(x,y), d_2(x,y), d_3(x,y)$
Complete Data mythical:	
True unaberrated image (object):	$o(z,w)$
Simulated image (intensity):	$i_1(x,y), i_2(x,y), i_3(x,y)$
Point Spread Function:	$h(x-z, y-w)$
Pixels, or image size:	N
Polarization parameter:	$P(z,w)$
Transmission of 3 polarizers:	$1/2$ —

Step 1: Obtain Statistical Model for the Measured Data

—	(1)
Note: only half of the light is unpolarized, since the polarizer cuts half out	
—	(2)
—	(3)

	(4)
--	-----

Step 2: Invent a set of Mythical Data (Complete Data)

	(5)
	(6)
Where unpolarized complete data is the same so,	(7)

Step 3: Select a Statistical Model for the Complete Data

Note: data chosen to be Poisson because the sum of Poisson random variables is a Poisson random variable

<p>—</p> <p>Where $P(z,w)=0$ in unpolarized case</p>	(8)
	(9)
	(10)

(11)

Step 4: Formulate the Complete Data Log-Likelihood

(12)

(13)

(14)

	(15)
	(16)
	(17)
	(18)

MAP (Maximum a Posteriori) Estimation: MAP Estimation is used because the polarization information is known prior to maximization calculations. MAP Estimation will try to maximize , while Maximum Likelihood tries to maximize .

(19)

can be disregarded because it does not have the parameters: $P(z,w)$, $o(z,w)$, or $C(z,w)$, and vanishes when the derivative is taken in the Maximization step.

(20)

The higher the n value in the Super Gaussian PDF, the more it models a step function. In reality $P(z,w)$ must always be less than 1. This PDF is chosen because it can be modeled as step function to drop at one, therefore mathematically making it very unlikely to get a number greater than 1 for $P(z,w)$.

Step 5: Expected Value

	(21)
--	------

Aside: $d = d1+d2$, where d is true measured data, $d1 \equiv$ one instance of a given sum, $d2 \equiv$ all other instances of the sum $\therefore d$ is a sum of measured data.
Now equate:

(22)

(23)

Refer to EQNs 1-3 for $E[d]$

_____	(24)
	(25)
	(26)
	(27)
_____	(28)

	(29)
	(30)
	(31)
	(32)
	(33)
	(34)
	(35)

(36)

(37)

Substitute EQNs 29-32 into 38-41 respectively:

(38)

(39)

(40)

(41)

Step 6: Maximization

<p>_____</p>	(42)
<p>_____</p>	(43)
<p>_____</p>	(44)
<p>_____</p>	(45)
<p>_____</p>	(46)

A - 49

	(47)
	(48)
	(49)
	(50)
	(51)
	(52)

\dots	(53)
---------	------

Algebra to simplify $o(z_0, w_0)$:

\dots Note: $h = 1$ due to the (refer to Rule of PSF's note above EQU 47)	(54)
--	------

\dots	(55)
---------	------

\dots	(56)
---------	------

Now differentiate only $Q4$ with respect to $C_3(z_0, w_0)$:

\dots	(57)
---------	------

\dots	(58)
---------	------

Now differentiate Q with respect to $P(z_0, w_0)$:

\dots	(59)
---------	------

$\frac{C_1}{C_2} = \frac{C_1}{C_2}$	(60)
$\frac{C_1}{C_2} = \frac{C_1}{C_2}$	(61)
$\frac{C_1}{C_2} = \frac{C_1}{C_2}$	(62)

Canceling out C_1 and C_2 terms:

$\frac{C_1}{C_2} = \frac{C_1}{C_2}$	(63)
$\frac{C_1}{C_2} = \frac{C_1}{C_2}$	(64)

Combine the four remaining terms:

$\frac{C_1}{C_2} = \frac{C_1}{C_2}$	(65)
$\frac{C_1}{C_2} = \frac{C_1}{C_2}$	(66)
$\frac{C_1}{C_2} = \frac{C_1}{C_2}$	(67)

$\frac{\partial}{\partial \alpha} \left(\frac{1}{\alpha} \right) = -\frac{1}{\alpha^2}$	(68)
	(69)

Last Step: Substitute EQU 56 into EQU 68

$\frac{\partial}{\partial \alpha} \left(\frac{1}{\alpha} \right) = -\frac{1}{\alpha^2}$	(70)
$\frac{\partial}{\partial \alpha} \left(\frac{1}{\alpha} \right) = -\frac{1}{\alpha^2}$	(71)
Note: Ignore common denominator, because the main idea of maximization after taking the derivative of all the Q terms is to set _____ equal to zero. This happens when the numerators are equal to zero.	(72)
	(73)
	(74)

Appendix B: Derivation for Assumed Poisson Noise in Richardson Lucy Algorithm

(Provided by: Dr. Stephen Cain, ENG780-Statistical Optics Class Notes)

Deconvolution with Poisson Noise

$$i(z, w) = \sum_{x=1}^N \sum_{y=1}^N o(x, y) h(z - x, w - y)$$

$$d(z, w) = i(z, w) + q(z, w)$$

$$P[d(z, w)] = \frac{i(z, w)^{d(z, w)} e^{-i(z, w)}}{d(z, w)!}$$

$$P[d(z, w) \forall (z, w) \in (1, N)] = \prod_{z=1}^N \prod_{w=1}^N \frac{i(z, w)^{d(z, w)} e^{-i(z, w)}}{d(z, w)!}$$

$$L(o) = \sum_{z=1}^N \sum_{w=1}^N d(z, w) \ln(i(z, w)) - i(z, w)$$

Deconvolution with Poisson Noise

$$L(o) = \sum_{z=1}^N \sum_{w=1}^N d(z, w) \ln(i(z, w)) - i(z, w)$$

$$\frac{\partial L(o)}{\partial o(x_o, y_o)} = \sum_{z=1}^N \sum_{w=1}^N \frac{\partial}{\partial o(x_o, y_o)} d(z, w) \ln(i(z, w)) - \frac{\partial i(z, w)}{\partial o(x_o)}$$

$$\frac{\partial}{\partial o(x_o, y_o)} d(z, w) \ln(i(z, w)) = d(z, w) \frac{\partial}{\partial o(x_o, y_o)} \ln(i(z, w))$$

$$\frac{\partial}{\partial o(x_o, y_o)} \ln(i(z, w)) = \frac{1}{i(z, w)} \frac{\partial i(z, w)}{\partial o(x_o, y_o)}$$

$$\frac{\partial i(z, w)}{\partial o(x_o, y_o)} = \sum_{x=1}^N \sum_{y=1}^N \frac{\partial}{\partial o(x_o, y_o)} o(x, y) h(z - x, w - y)$$

$$\frac{\partial}{\partial o(x_o, y_o)} o(x, y) = \delta(x - x_o, y - y_o)$$

$$\frac{\partial i(z, w)}{\partial o(x_o, y_o)} = \sum_{x=1}^N \sum_{y=1}^N \delta(x - x_o, y - y_o) h(z - x, w - y) = h(z - x_o, w - y_o)$$

Deconvolution with Poisson Noise

$$L(o) = \sum_{z=1}^N \sum_{w=1}^N d(z, w) \ln(i(z, w)) - i(z, w)$$

$$\frac{\partial L(o)}{\partial o(x_o, y_o)} = \sum_{z=1}^N \sum_{w=1}^N \frac{d(z, w)}{i(z, w)} h(z - x_o, w - y_o) - 1$$

$$\frac{\partial L(o)}{\partial o(x_o, y_o)} = \frac{\partial L^+(o)}{\partial o(x_o, y_o)} - \frac{\partial L^-(o)}{\partial o(x_o, y_o)}$$

$$\frac{\partial L^+(o)}{\partial o(x_o, y_o)} = \sum_{z=1}^N \sum_{w=1}^N \frac{d(z, w)}{i(z, w)} h(z - x_o, w - y_o)$$

$$\frac{\partial L^-(o)}{\partial o(x_o, y_o)} = 1$$

$$o^{new}(x, y) = o^{old}(x, y) \frac{\frac{\partial L^+(o)}{\partial o(x_o, y_o)}}{\frac{\partial L^-(o)}{\partial o(x_o, y_o)}}$$

8. Bibliography

- [1] Dempster, A. P., N. M. Laird, and D. B. Rubin, "Maximum likelihood from incomplete data via the EM algorithm," *J. Royal. Statistical Society B*, Vol. 39, No. 1, 1-37, 1977.
- [2] Goodman, Joseph W. *Statistical Optics*. New York: John Wiley & Sons, Wiley classics library edition, 2000
- [3] ----. *Introduction to Fourier Optics* (3rd Edition). Colorado: Roberts & Company Publishers, 2007.
- [4] Hecht, Eugene. *Optics* (4th Edition). California: Addison Wesley, 2002
- [5] Hyde, M, S. Cain, J. Schmidt, M. Havrilla. "Material classification of an unknown object using turbulence-degraded polarimetric imagery". *IEEE Transactions on Geoscience and Remote Sensing*, Vol. 49, No. 1, 264-276 (January 2011)
- [6] James, Stephen P. *Blind Deconvolution Through Polarization Diversity of Long Exposure Imagery*. Master's thesis, Air Force Inst of Tech, Wright Patterson Air Force Base, Ohio, March 2009.
- [7] Kay, Steven M. *Fundamentals of Statistical Signal Processing Estimation Theory* (Vol. 1). New Jersey: Prentice Hall PTR, 1993.
- [8] LeMaster, Daniel A. *Statistical Processing Methods for Polarimetric Imagery*. Ph.D. thesis, Air Force Inst of Tech, Wright Patterson AFB, Ohio, September 2008.
- [9] Leon-Garcia, Alberto. *Probability, Statistics and Random Processes for Electrical Engineering* (3rd Edition). New Jersey: Pearson Prentice Hall, 2008.
- [10] Lucy, L.B. "An Iterative Technique for the Rectification of Observed Distributions". *The Astronomical Journal*, Vol. 79, No. 6, 745-754 (June 1974)
- [11] Richardson, William H. "Bayesian-Based Iterative Method of Image Restoration". *J. Optical Society of America*, Vol. 62, No. 1, 55-59 (January 1972)
- [12] Richmond, Richard D. and Stephen C. Cain. *Direct Detection LADAR Systems*. Washington: SPIE, 2010
- [13] Schulz, Timothy J. "Multiframe blind deconvolution of astronomical images," *J. Optical Society of America A*, Vol. 10, No. 5, 1064-1073 (May 1993).
- [14] Shepp, L. and Y. Vardi. "Maximum likelihood reconstruction for emission tomography". *IEEE Transactions on Medical Imaging*, Vol. MI-1, No. 2, 113-122 (October 1982)
- [15] Strong, David M. *Polarimeter Blind Deconvolution Using Image Diversity*. Ph.D. thesis, Air Force Inst of Tech, Wright Patterson AFB, Ohio, September 2007.
- [16] Air Force Maui Optical & Supercomputing Site, Available: <http://www.maui.afmc.af.mil/about.html>

REPORT DOCUMENTATION PAGE				Form Approved OMB No. 074-0188	
<p>The public reporting burden for this collection of information is estimated to average 1 hour per response, including the time for reviewing instructions, searching existing data sources, gathering and maintaining the data needed, and completing and reviewing the collection of information. Send comments regarding this burden estimate or any other aspect of the collection of information, including suggestions for reducing this burden to Department of Defense, Washington Headquarters Services, Directorate for Information Operations and Reports (0704-0188), 1215 Jefferson Davis Highway, Suite 1204, Arlington, VA 22202-4302. Respondents should be aware that notwithstanding any other provision of law, no person shall be subject to a penalty for failing to comply with a collection of information if it does not display a currently valid OMB control number.</p> <p>PLEASE DO NOT RETURN YOUR FORM TO THE ABOVE ADDRESS.</p>					
1. REPORT DATE (DD-MM-YYYY) 07-03-2011		2. REPORT TYPE Thesis		3. DATES COVERED (From – To) May 2009 – Mar 2011	
4. TITLE AND SUBTITLE Three Channel Polarimetric Based Data Deconvolution				5a. CONTRACT NUMBER	
				5b. GRANT NUMBER	
				5c. PROGRAM ELEMENT NUMBER	
6. AUTHOR(S) Kurtis Engelson				5d. PROJECT NUMBER ENG 10304	
				5e. TASK NUMBER	
				5f. WORK UNIT NUMBER	
7. PERFORMING ORGANIZATION NAMES(S) AND ADDRESS(S) Department of Electrical and Computer Engineering Air Force Institute of Technology 2950 Hobson Way Wright Patterson AFB, OH 45433 Stephen.cain@afit.edu				8. PERFORMING ORGANIZATION REPORT NUMBER AFIT/GE/ENG/11-10	
9. SPONSORING/MONITORING AGENCY NAME(S) AND ADDRESS(ES) AFRL/RDSMA 535 Lipoa Pkwy, suite 200 Kihei, HI 96753 EMAIL:casey.pellizzari@maui.afmc.af.mil				10. SPONSOR/MONITOR'S ACRONYM(S) AFRL/RDSMA	
				11. SPONSOR/MONITOR'S REPORT NUMBER(S)	
12. DISTRIBUTION/AVAILABILITY STATEMENT APPROVED FOR PUBLIC RELEASE; DISTRIBUTION UNLIMITED. This material is declared a work of the U.S. Government and is not subject to copyright protection in the United States.					
13. SUPPLEMENTARY NOTES					
14. ABSTRACT A three channel polarimetric deconvolution algorithm was developed to mitigate the degrading effects of atmospheric turbulence in astronomical imagery. Tests were executed using both simulation and laboratory data. The resulting efficacy of the three channel algorithm was compared to a recently developed two channel approach under identical conditions ensuring a fair comparison amongst both algorithms. Two types of simulations were performed. The first was a binary star simulation to compare resulting resolutions between the three and two channel algorithms. The second simulation measured how effective both algorithms could deconvolve a blurred satellite image. The simulation environment assumed the key parameters of Fried's Seeing parameter, , and telescope lens diameters of and . The simulation results showed that the three channel algorithm always reconstructed the true image as good as or better than the two channel approach, while the total squared error was always significantly better for the three channel. The next step is comparing the two algorithms in the laboratory environment. However, the laboratory imagery was not actually blurred by atmospheric turbulence, but instead camera defocusing was used to simulate the blurring that would be caused by atmospheric turbulence. The results show that the three channel significantly outperforms the two channel in a visual reconstruction of the true image.					
15. SUBJECT TERMS Polarimetry, Deconvolution, Expectation Maximization					
16. SECURITY CLASSIFICATION OF:			17. LIMITATION OF ABSTRACT UU	18. NUMBER OF PAGES 67	19a. NAME OF RESPONSIBLE PERSON Dr. Stephen Cain
REPORT U	ABSTRACT U	c. THIS PAGE U			19b. TELEPHONE NUMBER (Include area code) 937-255-3636 x4716 stephen.cain@afit.edu

Standard Form 298 (Rev: 8-98)

Prescribed by ANSI Std. Z39-18